JGR Solid Earth

RESEARCH ARTICLE
10.1029/2019JB017589

Micromechanical Behavior of DNA-1A Lunar Regolith Simulant in Comparison to Ottawa Sand

C. S. Sandeep[1], V. Marzulli[2], F. Cafaro[3], K. Senetakis[1], and T. Pöschel[2]

[1]Department of Architecture and Civil Engineering, City University of Hong Kong, Kowloon Tong, Hong Kong, [2]Institute for Multiscale Simulations, Friedrich-Alexander-Universität Erlangen-Nürnberg, Erlangen, Germany, [3]DICATECh – Technical University of Bari, Bari, Italy

Key Points:
- The interface properties of DNA-1A lunar regolith simulant and Ottawa sand were studied with an advanced grain-scale apparatus
- DNA-1A had much lower normal contact stiffness but higher interparticle friction angles compared with Ottawa sand
- Analytical model by Yimsiri and Soga (2000, https://doi.org/10.1680/geot.2000.50.5.559) in the normal direction fits well the experimental curves for the entire span of displacements

Supporting Information:
- Supporting Information S1
- Data Set S1

Correspondence to:
K. Senetakis,
ksenetak@cityu.edu.hk

Citation:
Sandeep, C. S., Marzulli, V., Cafaro, F., Senetakis, K., & Pöschel, T. (2019). Micromechanical behavior of DNA-1A lunar regolith simulant in comparison to Ottawa sand. *Journal of Geophysical Research: Solid Earth*, *124*. https://doi.org/10.1029/2019JB017589

Received 25 FEB 2019
Accepted 28 JUL 2019
Accepted article online 1 AUG 2019

Abstract In this study, the micromechanical interparticle contact behavior of "De NoArtri" (DNA-1A) grains is investigated, which is a lunar regolith simulant, using a custom-built micromechanical loading apparatus, and the results on the DNA-1A are compared with Ottawa sand which is a standard quartz soil. Material characterization is performed through several techniques. Based on microhardness intender and surface profiler analyses, it was found that the DNA-1A grains had lower values of hardness and higher values of surface roughness compared to Ottawa sand grains. In normal contact micromechanical tests, the results showed that the DNA-1A had softer behavior compared with Ottawa sand grains and that cumulative plastic displacements were observed for the DNA-1A simulant during cyclic compression, whereas for Ottawa sand grains elastic displacements were dominant in the cyclic sequences. In tangential contact micromechanical tests, it was shown that the interparticle friction values of DNA-1A were much greater than that of Ottawa sand grains, which was attributed to the softer contact response and greater roughness of the DNA-1A grains. Widely used theoretical models both in normal and tangential directions were fitted to the experimental data to obtain representative parameters, which can be useful as input in numerical analyses which use the discrete element method.

Plain Language Summary Lunar regolith simulants comprise natural soils found on Earth or artificially created materials which mimic the properties of the real lunar surface soil. Understanding the behavior of these simulants can help researchers to prepare for further explorations and settling of facilities on the Moon. In this study, an attempt is made to examine in the laboratory the behavior of the lunar regolith simulant "De NoArtri" (DNA-1A), and the results are compared with a standard soil of quartz grains to understand the differences and obtain insights into the properties of the lunar simulant. The behavior of regolith simulant is compared with Ottawa sand grains to understand the differences between these two materials in terms of material properties as well as micromechanical behavior. This micromechanical behavior gives a fundamental understanding of the mechanical response of the material and can provide important parameters to be further utilized in computer simulations so that settling of facilities on the Moon surface can be designed safely.

1. Introduction

The European Space Agency's Moon village idea involves the planning of lunar settlement with a possible multinational collaboration. Private space-flight companies such as SpaceX and Virgin Galactic are investing billions of dollars to provide a feasible space travel. Meurisse et al. (2017) stated that the utilization of lunar materials is a cost-effective solution to build shelters, roads, or even launch pads for rockets on the Moon. The knowledge of the geological and mechanical properties of the lunar regolith is needed to further design/improve the structures, lunar roving vehicle, and other autonomous vehicle designs or the design of launching pads (Hill et al., 2007; Horanyi et al., 1998).

Lunar regolith simulant is an alternative form of material, which has very similar chemical, mechanical, mineralogical, particle distribution, and engineering properties of that of lunar regolith (McKay et al., 1994). The DNA simulant was used by the European Space Agency to manufacture lunarcrete by using the three-dimensional printing technology and to perform experiments on construction of building blocks. Marzulli and Cafaro (2019) studied the geotechnical properties of the DNA-1A simulant in a loose and uncompacted state in order to understand the behavior of the material with applications in the operation of rover vehicles for earthworks. The lunar regolith consists of discrete particles and it can be classified as

Table 1
Chemical Composition of DNA-1 (After Cesaretti et al., 2014), DNA-1A, LBS, and Ottawa Sand (OS) Using EDS Analysis

Oxide	DNA-1 (wt %)	DNA-1A (wt %)	LBS (wt %)	OS (wt %)
SiO_2	41.90	51.87	81.77	98.12
TiO_2	1.31	0.80	0.29	0.07
Al_2O_3	16.02	19.21	4.24	0.83
Fe_2O_3	14.60	8.30	8.22	0.23
MgO	6.34	2.84	1.63	0.55
CaO	12.90	5.41	0.48	-
Na_2O	2.66	5.76	1.88	0.20
K_2O	2.53	4.22	0.81	-
MnO	0.21	0.22	0.68	-
P_2O_5	0.34	1.39	-	-

a granular material (Hasan & Alshibli, 2010) which does not contain organic matter (NASA, 2018). There is particular interest in the study of the behavior of the lunar regolith at low effective stresses, but such experiments are difficult to be performed in the laboratory due to the effect of terrestrial gravity and the models used should be scaled for Moon's gravitational acceleration (Cafaro et al., 2018; Hasan & Alshibli, 2010; Sture et al., 1998). Hence, cost-effective numerical modeling tools such as the discrete element method (DEM; after Cundall & Strack, 1979) have been implemented for the simulation of the lunar regolith and its interactions with rover vehicles (Knuth et al., 2012; Li et al., 2010; Nakashima et al., 2010, 2011; Sullivan et al., 2011) and retaining structures (Jiang et al., 2016).

The analysis at the grain scale has helped researchers to improve their understanding on the complex behavior of granular materials and analyze multiscale problems (Guo & Zhao, 2016; O'Sullivan, 2011; Soga & O'Sullivan, 2010). The parameters obtained through micromechanical tests at the grain scale (for example, interparticle friction, normal and tangential stiffness) comprise important input in numerical simulations using DEM analyses, for example, in the analysis of the macroscale response of granular materials subjected to monotonic or cyclic loading and the flowability behavior of granular materials (Huang et al., 2014; Iverson et al., 2011; Sazzad & Suzuki, 2011; Yan et al., 2015). Based on this, significant advancements took place in recent years in microscale experimentation investigating the contact behavior of geological materials and lunar regolith simulants (e.g., Cavarretta et al., 2010; Cole, 2015; Cole & Peters, 2008; Nardelli et al., 2017; Nardelli & Coop, 2018; Sandeep & Senetakis, 2018a, 2018b, 2019; Senetakis et al., 2013a, 2013b; Senetakis & Coop, 2014). It is highlighted, based on the studies by Sandeep and Senetakis (2018c, 2018d), that the mesoscale morphology of the grains and the previous loading history affect, markedly, the interparticle load-displacement relationship and coefficient of friction.

In this study, the interparticle contact behavior of DNA-1A lunar regolith simulant was investigated using a custom-built micromechanical loading apparatus investigating both compression and shearing behavior at the grain contacts. In order to obtain insights into the grain-scale behavior of the regolith simulant, the experimental results were compared with tests performed on Ottawa sand (OS) grains, which sand can be considered as a benchmark material. The experimental results were compared with the widely used Hertz (1882) and Yimsiri and Soga (2000) models in the normal direction and with the models proposed by Mindlin and Deresiewicz (1953) and Dahl (1976) in the tangential direction. These comparisons are made to obtain the model parameters which can be used in numerical analyses for realistic simulations of granular assemblies.

2. Materials

2.1. General Description and Origin of DNA-1A and Ottawa Sand

In the study, a lunar regolith simulant (DNA-1A) and Ottawa sand grains were examined using several techniques. DNA-1A has the same origin as the DNA-1 simulant tested by Cesaretti et al. (2014). Basic characterization of these two materials was previously reported by Marzulli and Cafaro (2019) and Erdogan et al. (2017). The simulant was prepared from ash which was mined from a commercial cinder quarry at Onano (north flank of Bolsena Crater, Italy). The ash was coarse sieved prior to the crunching in an impact mill after which it was allowed to partially dry in air. Thereafter, the material was grinded and sieved through a 0.125 UNI2332 sieve to form a final mix having average water content around 1.7% in weight. The specific gravity of solids (G_S) of the DNA-1A and Ottawa sand materials is 2.70 and 2.65, respectively, which values are determined by the water pycnometer method (after Marzulli & Cafaro, 2019, Winters et al., 2007). The particle size of DNA-1A and Ottawa sand grains used in this study ranged between 1.00–1.80 and 0.50–0.80 mm, respectively. The finer content of the DNA-1A has not been tested due to technical difficulties: the entire grain size distribution of this lunar simulant can be found in Marzulli and Cafaro (2019).

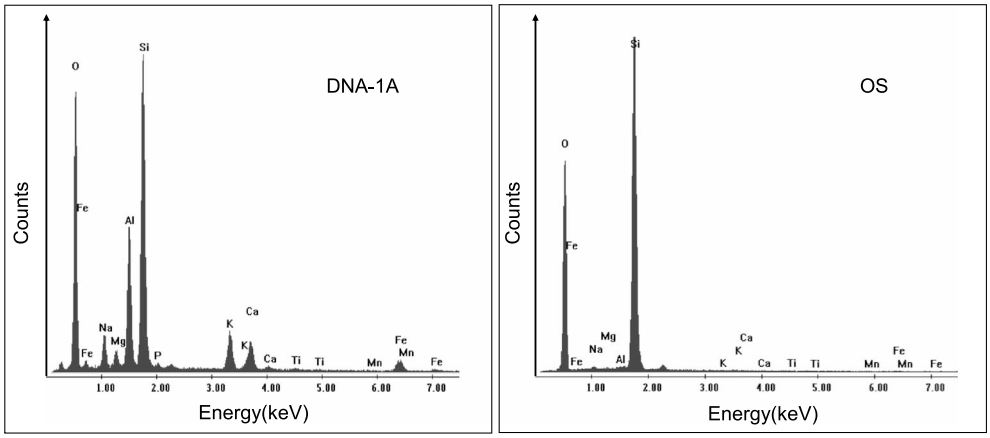

Figure 1. Representative EDS spectrum of DNA-1A and Ottawa sand (OS).

2.2. Chemical and Mineralogical Composition

The chemical analysis of the materials was conducted using energy-dispersive X-ray spectroscopy analysis, and the average values from four measurements, for each material type, are reported in Table 1. Representative energy-dispersive X-ray spectroscopy spectrum results of DNA-1A and Ottawa sand grains are presented in Figure 1. The chemical composition of DNA-1 presented by Cesaretti et al. (2014) and Leighton Buzzard sand (LBS) presented by Sandeep and Senetakis (2018a) are also summarized in Table 1 for comparison purposes. Based on the chemical analysis from Table 1 and Figure 1, it can be concluded that the composition of DNA-1A is very similar to that reported by Marzulli and Cafaro (2019). In general, due to the absence of atmosphere on the Moon, the iron is present in the form of Fe_2 and FeO (Markandeya Raju & Pranathi, 2012) on the real lunar regolith. However, for the regolith simulants low content of Fe_2O_3 has been observed, in specific 14.60% for DNA-1, 8% for DNA-1A (this study), 6% for BP-1 (Black Point-1), and 3.41% for JSC-1A (after Cesaretti et al., 2014; Rickman et al., 2007; Suescun-Florez et al., 2014).

Using polarized light microscopy and X-ray powder diffraction, Erdogan et al. (2017) reported that Ottawa sand grains have single crystals of α-quartz. The chemical analysis in the present study (Table 1) shows that Ottawa sand grains are rich in SiO_2 (98%) compared to LBS (82%) and DNA-1A (52%). Ottawa sand grains are white to transparent in color, whereas LBS grains are usually yellowish to brown in color which is majorly attributed to the presence of Fe_2O_3 (8%) on the surfaces of LBS.

2.3. Scanning Electron Microscope Images

Figures 2a–2d show representative scanning electron microscope images of DNA-1A and Ottawa sand grains at different magnifications (50X, 1,000X, and 5,000X). The images in Figures 2a and 2b indicate the vesicular structure and irregular shape with sharp corners of the DNA-1A grains. The DNA-1A grains can be visually classified as subprismoidal with subangular to angular shape according to Powers (1982) chart. The milling process used to grind the DNA-1A simulant might be responsible for these observations in particle morphology. The vesicles, which are irregular in shape, are generated by gases during the cooling of magma. Observations at higher magnifications show that the irregular-shaped clasts ranging from 5 to 10 μm in diameter are attached to each other. In general, a good resemblance observed between DNA-1A particles and images of JSC-1A regolith (Alshibli & Hasan, 2009) and lunar regolith (Carrier, 2003) in terms of angular shape with sharp corners and crevices on the surface. One major difference between the lunar regolith and its simulant is the presence of interparticle adhesion in the original Moon material (Costes & Mitchell, 1970; Suescun-Florez et al., 2014), which might be due to the different specific surfaces of the particles formed in different environmental conditions (Marzulli & Cafaro, 2019).

Figures 2c and 2d show images of Ottawa sand grains which are fairly regular in shape compared to DNA-1A. Ottawa sand grains can be classified as subprismoidal to spherical with rounded to well-rounded shape according to Powers (1982) chart. The grains are relatively smaller in size compared to DNA-1A, and there

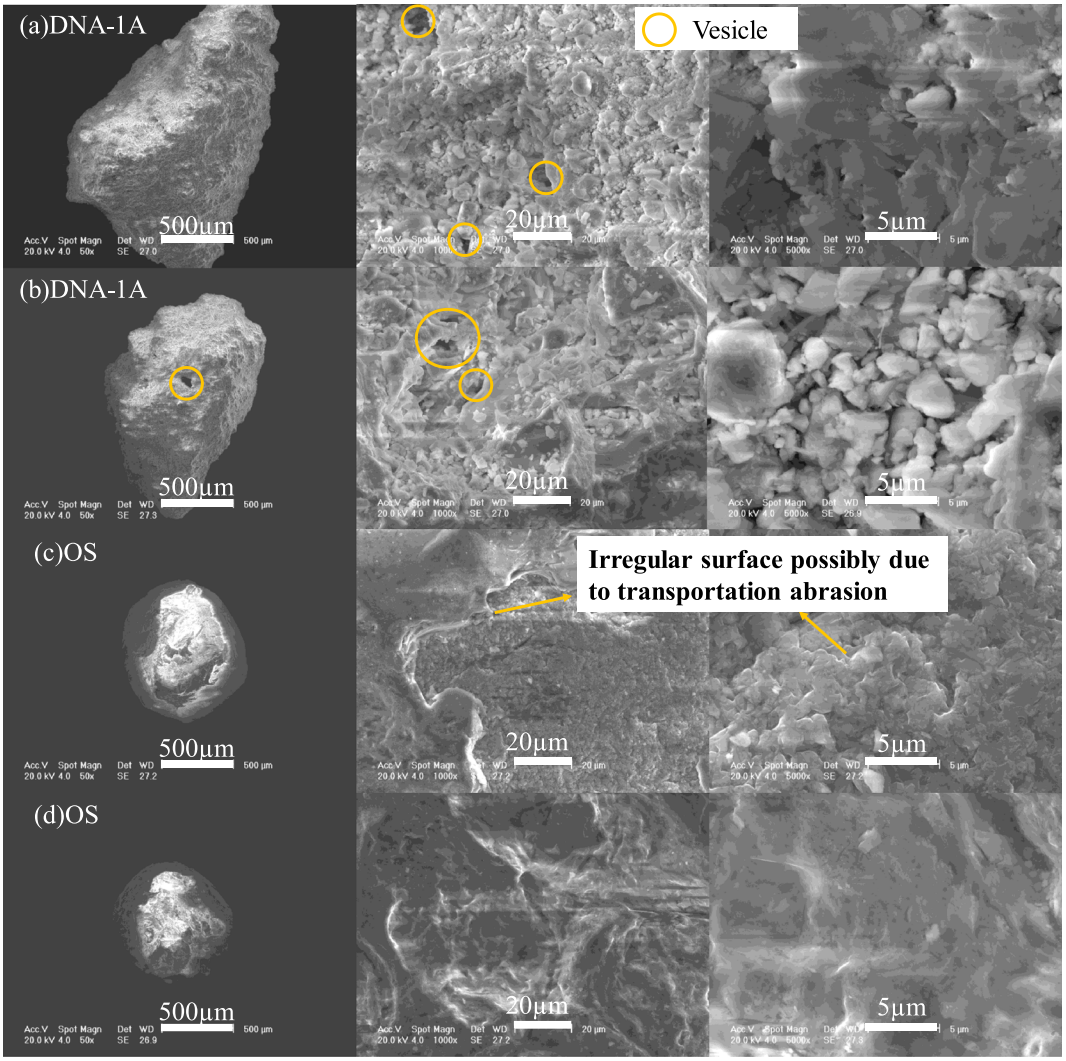

Figure 2. Representative SEM images at different magnifications. (a and b) Sharp-edged DNA-1A simulant grains with visible irregular vesicles on the surface. (c and d) Rounded Ottawa sand (OS) grains showing irregular surfaces possibly due to transportation abrasion.

are minor abrasions visible on their surfaces which might be due to the sediment transportation (Ghosh et al., 2014). Similar abrasions were also observed by Sandeep, He, et al. (2018) on the surfaces of river sand grains from Guangdong Province, China.

2.4. Surface Roughness

The surface roughness of the materials was measured using the Veeco NT9300 optical surface profiler. The vertical scanning interferometry mode was used for the DNA-1A grains due to its ability to measure surface roughness over large scan areas of a heterogeneous surface (Conroy & Mansfield, 2008). The phase shifting interferometry mode was used to determine the surface roughness of Ottawa sand grains. The phase shifting interferometry mode is very precise and normally used to measure surface roughness of smooth and continuous surfaces. Nevertheless, both modes correspond to nondestructive evaluation of the surface roughness. A field of view of 20 × 20 µm was chosen similar to previous studies (Senetakis et al., 2013b, 2017), and the effect of curvature was removed prior to the determination of surface roughness (i.e., roughness was measured on flattened areas). The surface roughness was presented in the form of root-mean-square roughness

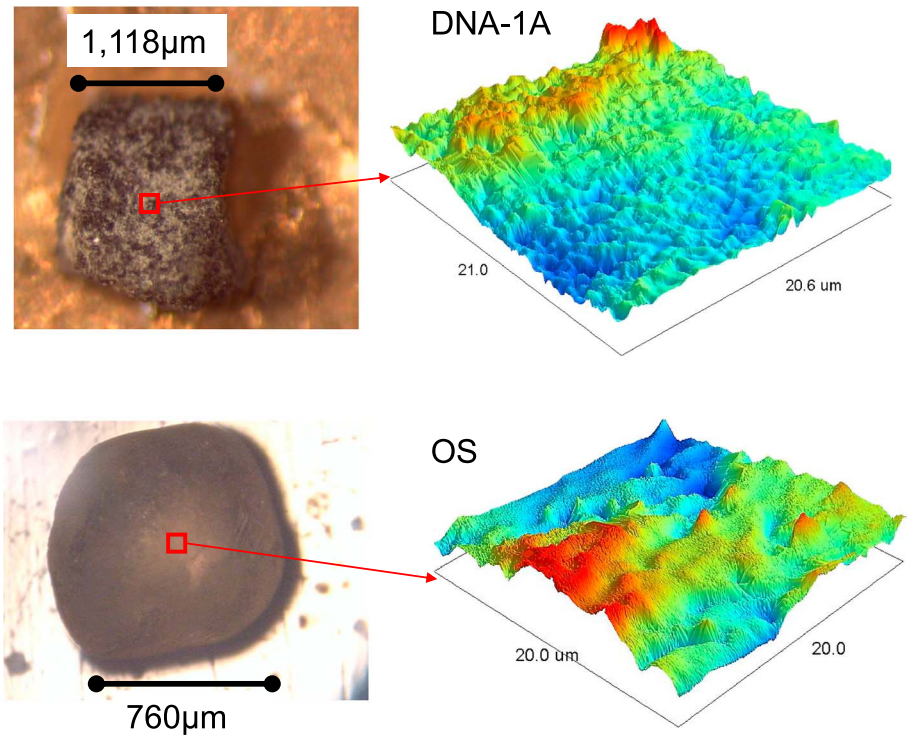

Figure 3. Microscope images and flattened three-dimensional surface roughness profiles of DNA-1A and Ottawa sand (OS).

(S_q) based on equation (1). The S_q is more sensitive in determining the peaks and valleys, which is better for different surface types (De Oliveira et al., 2012; Gadelmawla et al., 2002).

$$S_q = \sqrt{\frac{1}{u}\sum_{i=1}^{u}\left(W_i^2\right)} \tag{1}$$

where u represents the number of measured data points and W is the elevation relative to the base surface. Typical flattened three-dimensional surface roughness profiles of DNA-1A and Ottawa sand grains are shown in Figure 3. It was observed from Figure 3 that the Ottawa sand grains are much smoother than the crushed DNA-1A samples. The average S_q values of the DNA-1A (10 measurements) and Ottawa sand grains (four measurements) are 1,476 ± 379 and 204 ± 42 nm, respectively. The surface roughness of DNA-1A is relatively high and it is comparable with the surface roughness of grains from completely decomposed granite (1,341 ± 390 nm) and decomposed volcanic tuff (1,770 ± 689 nm; after Sandeep & Senetakis, 2018b; Sandeep, Todisco, et al., 2018). The Ottawa sand grains have lower values of surface roughness and they are similar to the LBS grains in terms of S_q value (223 ± 61 nm; Sandeep & Senetakis, 2018b). The high roughness of DNA-1A grains can be probably attributed to both syngenetic characters of the ash and the grinding and crunching of the material during preparation. Similarly, Sandeep and Senetakis (2018d) reported high values of surface roughness for crushed limestone grains (670 ± 221), which they attributed to the material crushing.

2.5. Microhardness

The microhardness tests were conducted on a set of grains using the Fischer HM2000XY Micro-Hardness Tester. A sample holder was used to hold the grains so that the apex of the grains would be at the same level with the holder. Polishing and grinding of the grains were avoided as it might affect the residual stress state and microhardness values (Griepentrog et al., 2002; Todisco et al., 2017). A standard Vickers diamond

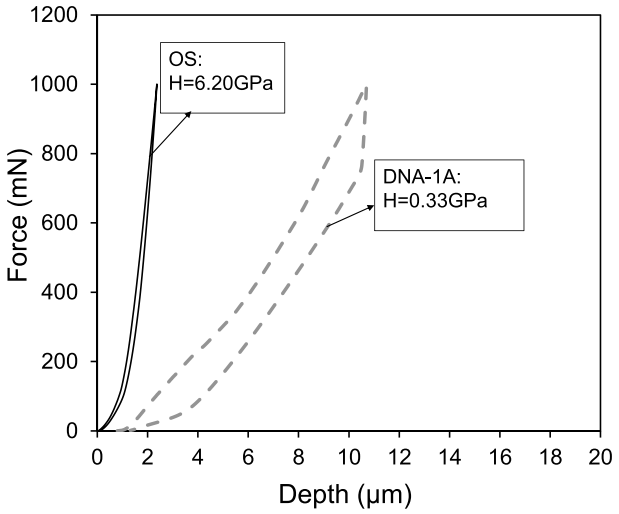

Figure 4. Representative curves showing normal force against indentation depth behavior during microhardness test for DNA-1A and Ottawa sand (OS) grains.

pyramid indenter with an angle (β) of 136° between its faces was used in the microhardness tests. The samples were indented using a force-controlled mode at a rate of 0.05 N/s. After reaching a normal force (F_N) of 1 N the samples were unloaded. Figure 4 shows representative normal force against indentation depth (F_N-h) curves for DNA-1A and Ottawa sand grains from the microhardness tests. The average values of microhardness for the tested materials referring to Martens hardness (H) are reported in Table 2, which were calculated as the ratio of the applied indentation force (F_N) to the surface area (A_S) of the indenter penetrating beyond the zero point of the contact (equations (2) and (3)).

$$H = \frac{F_N}{A_S} \tag{2}$$

$$A_S = \frac{4h^2 \sin\left(\frac{\beta}{2}\right)}{\cos^2\left(\frac{\beta}{2}\right)} \tag{3}$$

The average microhardness values (based on six tests for each material type) of DNA-1A and Ottawa sand were equal to 0.32 and 5.8 GPa, respectively, with a standard deviation of ±0.11 and ±0.90 GPa, respectively. Daphalapurkar et al. (2011) and Erdogan et al. (2017) using the nanoindentation technique reported hardness values of polished quartz sand grains ranging between 10 and 15 GPa. The average value of microhardness of Ottawa sand grains is similar in magnitude with the value reported by Todisco et al. (2017) for LBS grains (6.2 GPa). The hardness values from the present study for Ottawa sand grains are relatively lower in magnitude compared with previous studies (Daphalapurkar et al., 2011; Erdogan et al., 2017) which is attributed to the conduction of the experiments on natural surfaces in the present study rather than polished surfaces on Ottawa sand grains; thus, the presence of small asperities at the microscale (i.e., roughness) may decrease the resultant hardness.

3. Contact Mechanics Models

In DEM, the simulation of geological materials necessitates an understanding of the contact response at the interfaces of particles, which helps to choose proper input parameter values, for example, interparticle coefficient of friction, or constitutive laws such as normal and tangential force–displacement relationships for the discrete particles. In this section, a brief review is presented on a few contact models along with their corresponding parameters needed in DEM, which models have been used in the analytical part of the present study so that, based on the experimental results, useful equations and their parameters can be proposed to be implemented in numerical simulations of granular materials with focus on DNA-1A simulant and a standard quartz sand.

3.1. Normal Direction

3.1.1. Hertz Contact Model

Hertz (1882) proposed an elastic nonlinear contact model which is widely used in the simulation of the contact behavior in the normal direction. Figure 5a shows two identical spheres of radius "R" in contact subjected to a normal force (F_N) which generates a circular contact area of radius "a" which is expressed from equation (4).

$$a = \left(\frac{3\mathrm{RF_N}}{8E^*}\right)^{\frac{1}{3}} \tag{4}$$

where E^* is the equivalent Young's modulus which is expressed from equation (5). In equation (5), E and ν correspond to Young's modulus of the grains and the material Poisson's ratio, respectively (assuming that E and ν are same for top and bottom grains in contact).

Table 2
Properties of the Materials Tested

Property	DNA-1A	OS
Grain size (mm)	1.00–1.80	0.50–0.80
Specific gravity	2.70	2.65
Roughness (S_q) (nm)	1476 ± 379	204 ± 42
Hardness (H_M) (GPa)	0.32 ± 0.11	5.8 ± 0.90

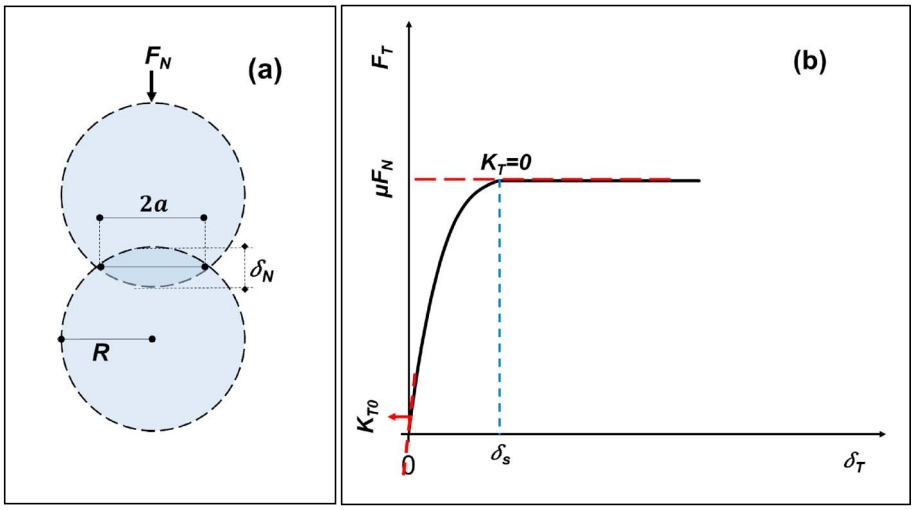

Figure 5. (a) Application of normal force along two identical spheres. (b) Idealized tangential force against displacement curve during monotonic shearing.

$$E^* = \frac{E}{2(1-\nu^2)} \tag{5}$$

The normal displacement, δ_N, is correlated with the contact radius and the radius of the grains through equation (6), while the normal force and normal displacement are correlated through equation (7) (Hertz, 1882; after Johnson, 1985).

$$\delta_N = 2\frac{a^2}{R} \tag{6}$$

$$F_N = \frac{2\sqrt{2}(R)^{\frac{1}{2}}E^*\delta_N^{\frac{3}{2}}}{3} \tag{7}$$

Previous works (Balevicius & Mroz, 2018; Cavarretta et al., 2010; Nardelli et al., 2017; Nardelli & Coop, 2018; Sandeep & Senetakis, 2018a, 2018c) showed that the theoretical curves plotted using the Hertz model fit the experimental data reasonably well apart from an initial regime where the behavior is elastic-plastic to plastic for rough surface morphologies.

3.1.2. Yimsiri and Soga Model

Yimsiri and Soga (2000) presented an analytical micromechanical model for rough surfaces to study the effect of fabric anisotropy, stress condition, and contact characteristics on the small-strain behavior of granular soils. They derived the model by assuming the soil as an assembly of uniform-sized spheres, and a fabric tensor was incorporated to define the packing structure of the spheres. The main assumptions of this model at small strains include no sliding between the soil particles, no particle spinning, and no resisting moment at the contact. Yimsiri and Soga studied the contact between the particles by incorporating three different contact laws namely, the linear elastic, Hertz-Mindlin, and rough surface contact models. The roughness of the surface is introduced into the model by considering a variation of asperity heights via a nondimensional roughness parameter (α). Through curve fitting of the data from Johnson (1985), Yimsiri and Soga (2000) showed that the radius ratio (a^*/a) is a hyperbolic function of αas presented in equation (8).

$$\frac{a^*}{a} = \frac{-2.8}{\alpha+2} + 2.4 \tag{8}$$

where a^* is the effective circular contact radius (rough surface).

Using micromechanics theory, they presented a link between interparticle force-displacement relationship to macroscopic stress-strain behavior. The morphological characteristics of the granular assembly (at the microscale) used in the simulations might substantially affect the predicted overall macroscopic behavior and that by taking into account the surface roughness, the numerical results are closer to the real behavior observed in laboratory tests (after Hu et al., 2010; Senetakis et al., 2013a; Yimsiri & Soga, 2000).

3.2. Tangential Direction

3.2.1. Mindlin and Deresiewicz Model

Cattaneo (1938) and Mindlin (1949) extended the theory proposed by Hertz (1882) (which was originally applied in the normal direction) by considering an increasing tangential force at the contact. Later Mindlin and Deresiewicz (1953) referred to as MD model, studied a special case of two elastic identical spheres in contact assuming that the normal pressure distribution and the contact area remain unchanged during shearing. This model predicts the initial part of the tangential force-displacement curve as nonlinear and after reaching a critical value of tangential force ($F_{TC} = \mu F_N$) the curve shows a purely plastic behavior (Figure 5b). In DEM simulations of granular materials Hertz and MD models are commonly used in the normal and tangential directions (e.g., Kermani et al., 2015; Yohannes et al., 2012). Mindlin and Deresiewicz (1953) proposed equations (9) and (10) to obtain the initial tangential stiffness(K_{T0}) and tangential stiffness at any displacement (K_{Tx}):

$$K_{T0} = \frac{8a}{N^*} \tag{9}$$

$$K_{Tx} = K_{T0}\left(1 - \frac{F_{Tx}}{\mu F_N}\right)^{\frac{1}{3}} \tag{10}$$

where N^* is expressed from equation (11) and G is the shear modulus of the materials in contact.

$$\frac{1}{N^*} = \frac{G}{2(2-\nu)} \tag{11}$$

The tangential force F_{T2} at any time step with an increase in tangential displacement $\Delta\delta_T$ is expressed from equation (12).

$$F_{T2} = F_{T1} + K_T \Delta\delta_T \tag{12}$$

where F_{T1} is the tangential force in the previous time step.

3.2.2. Dahl's Friction Model

Dahl (1976) developed a theory of solid friction where he described friction as a macroscopic result of quantum mechanical bonds between two contact surfaces. Dahl's friction model is a dynamic empirical model derived from material strain rate equation. He assumed that the friction is a function of velocity and displacement. He observed that during shearing an intermediate motion of one surface over another occurs before entering a macroscopic relative motion. Dahl's friction model is a typical simulation model used in the aerospace industry and for robotics to study wheel-tire interactions (Krid et al., 2017). Saltiel et al. (2017) mentioned that Dahl's model is simple, and it can capture velocity reversal and allows parameters to be compared to those commonly used to account for fault and earthquake nucleation behavior. The general form of Dahl's model is expressed from equation (13).

$$\frac{dF_T}{d\delta_T} = K_{T0}\left[1 - \frac{F_T}{F_{Tc}}\,\mathrm{sign}(u_T)\right]^{\chi} \mathrm{sign}\left[1 - \frac{F_T}{F_{Tc}}\,\mathrm{sign}(u_T)\right] \tag{13}$$

where K_{T0} is the experimentally derived initial tangential stiffness (N/mm), *sign* is the signum function, F_{Tc} is the critical value of tangential force, u_T is the velocity, and χ is a dimensionless parameter which

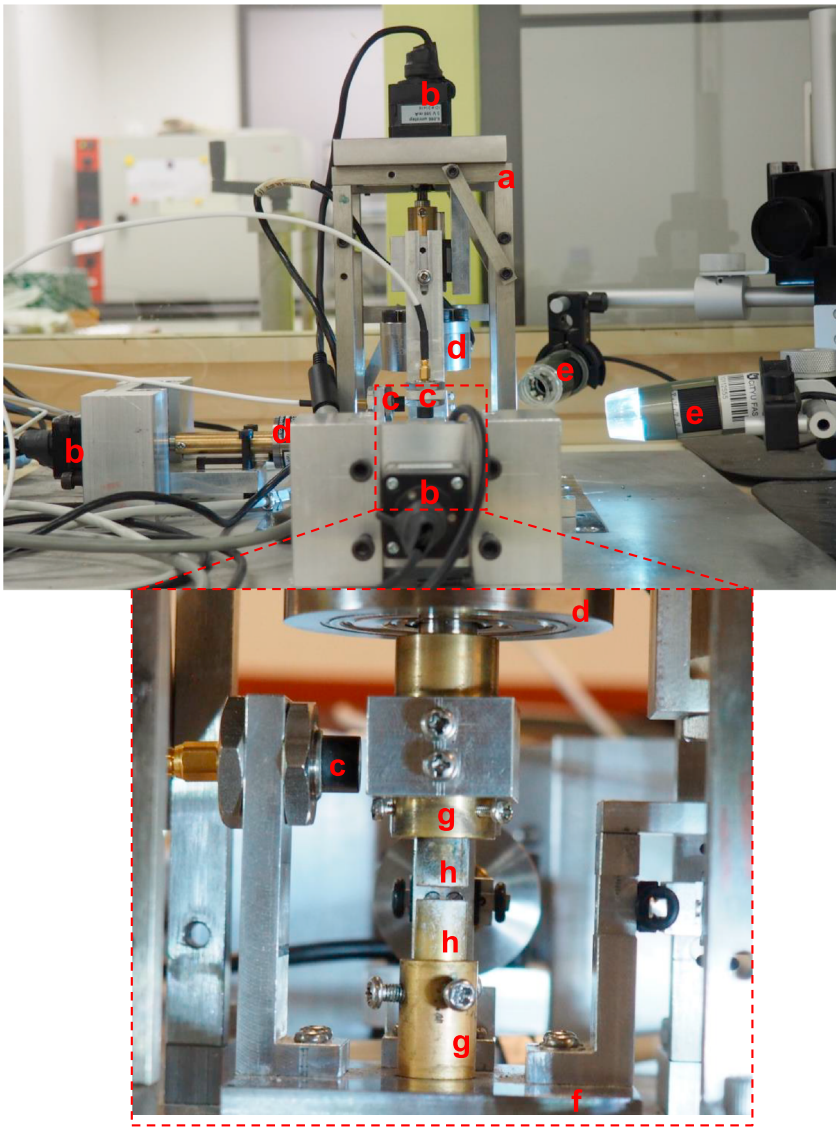

Figure 6. Image of the interparticle loading apparatus showing its different components. (a) Stainless steel frame. (b) Stepping motor. (c) Noncontact displacement sensor. (d) Load cell. (e) Microcamera. (f) Stainless steel sled. (g) Top and bottom wells. (h) Top and bottom mounts.

determines the shape of the tangential force against displacement curve. According to Dahl (1976), the value of χ determines the general form of friction functions, and varying values of χ can fit the force-displacement curves of both ductile and brittle materials.

4. Experimental Equipment and Testing Program

Figure 6 shows an image of the interparticle loading apparatus displaying its key components. The apparatus has been designed by Senetakis and Coop (2014) and upgraded by Nardelli et al. (2017). It consists of a stiff loading frame (a) and three loading arms in three orthogonal directions (for example, x, y, and z axes). Each loading arm consists of various parts which include a stepping motor (b), a noncontact eddy current displacement sensor with a repeatability of 10^{-5} mm (c), and a high-resolution load cell (d) of 100-N capacity with a repeatability of 0.02 N.

The grains (specimens) were glued using cyanoacrylate glue to the brass mounts (hr) of 8 mm in diameter and left to dry for a period of 12–24 hr before testing. After drying, the mounts were placed into both the top and bottom wells of the apparatus. The top well was located on the vertical arm and the bottom well was placed on the sled. The sled was positioned on a three-ball bearing system and it was allowed for movement in the horizontal plane. The whole apparatus was placed inside a Perspex chamber to maintain the humidity. All the tests in this testing program were performed at a room temperature of 23–25 °C. The apparatus was calibrated in both normal and tangential directions, and the experimental results were corrected for the stiffness of the apparatus and friction of the bearing systems.

The testing program consisted of 30 interparticle tests on both DNA-1A and OS grains, which includes 16 monotonic shearing tests, eight monotonic repeated shearing tests, two cyclic normal loading tests, and four cyclic shearing tests. The repeated shearing tests were performed to observe the changes in stiffness and loading response after the virgin compression and shearing were completed. The cyclic normal loading tests were performed to study the possible effects of various cycles on the plastic deformation and Young's modulus at the contacts of the grains. The cyclic shearing tests were carried out to quantify energy losses for different types of grains during shearing at different displacement amplitudes. The velocity of the tests was 0.2 mm/hr in normal compression experiments and 0.1 mm/hr in shearing experiments.

5. Results and Discussion

5.1. Normal Contact Behavior

5.1.1. Monotonic Compression

Representative normal force against displacement curves for DNA-1A and Ottawa sand pairs of grains during monotonic normal loading are given in Figure 7a. For most of the tests, the normal force increased nonlinearly with the displacement which is expected for the compression of apex-to-apex contact types based on Hertz theory (after Hertz, 1882). Some of the curves of the DNA-1A showed fluctuations or a significant drop of the normal force during the compression process which can be attributed, predominantly, to the brittle behavior and breakage of asperities during the application of the normal force. This behavior may be advanced because of the low hardness and rough surface morphology of the regolith simulant. For a given material type and displacement magnitude, the scatter in the normal force is, primarily, because of the differences in surface morphological features among different grains. This scatter in the data was greater, as expected, for the DNA-1A simulant, since this material exhibited greater scatter in its morphological and elastic characteristics compared with that of the Ottawa sand.

The experimental curves show that the Ottawa sand grains were much stiffer in the normal direction compared with the DNA-1A grains. From the highlighted part of Figure 7a, it was observed that both materials showed some plastic response in the initial regime of the curves, on the order of 0.2 to 0.8 μm for Ottawa sand and 1.1 to 5.1 μm for DNA-1A. For the Ottawa sand, this observed range of initial plastic displacements is very similar with previously reported data on Eglin sand by Nardelli et al. (2017) and LBS by Sandeep and Senetakis (2018a, 2018d). For the regolith simulant, the extended regime of initial plastic displacements is similar with the reported data on decomposed granite grains by Sandeep and Senetakis (2018b) and Nardelli and Coop (2018). The higher values of surface roughness and the brittle nature of the microasperities of the DNA-1A grains might have contributed to the observed trends. Based on the results from this study and from previous works by the authors (Sandeep & Senetakis, 2018a, 2018d) on other geological materials, the initial regime of plastic displacements qualitatively depends on surface roughness. However, a clear quantitative correlation was not observed for the tested materials between magnitude of initial plastic displacements and surface roughness.

Figure 7b shows representative normal stiffness against displacement curves of DNA-1A and Ottawa sand pairs of grains in comparison with JSC-1A and Eglin sand grains from previous studies (after Cole & Peters, 2008; Nardelli et al., 2017). The normal stiffness values of the DNA-1A grains were very low in magnitude compared with other materials, and Ottawa sand grains showed a nearly linear relationship between normal stiffness and displacement in the log-scale plot. As highlighted earlier, the low normal stiffness values of DNA-1A were attributed, predominantly, to the composition and the rough surface morphology of the grains.

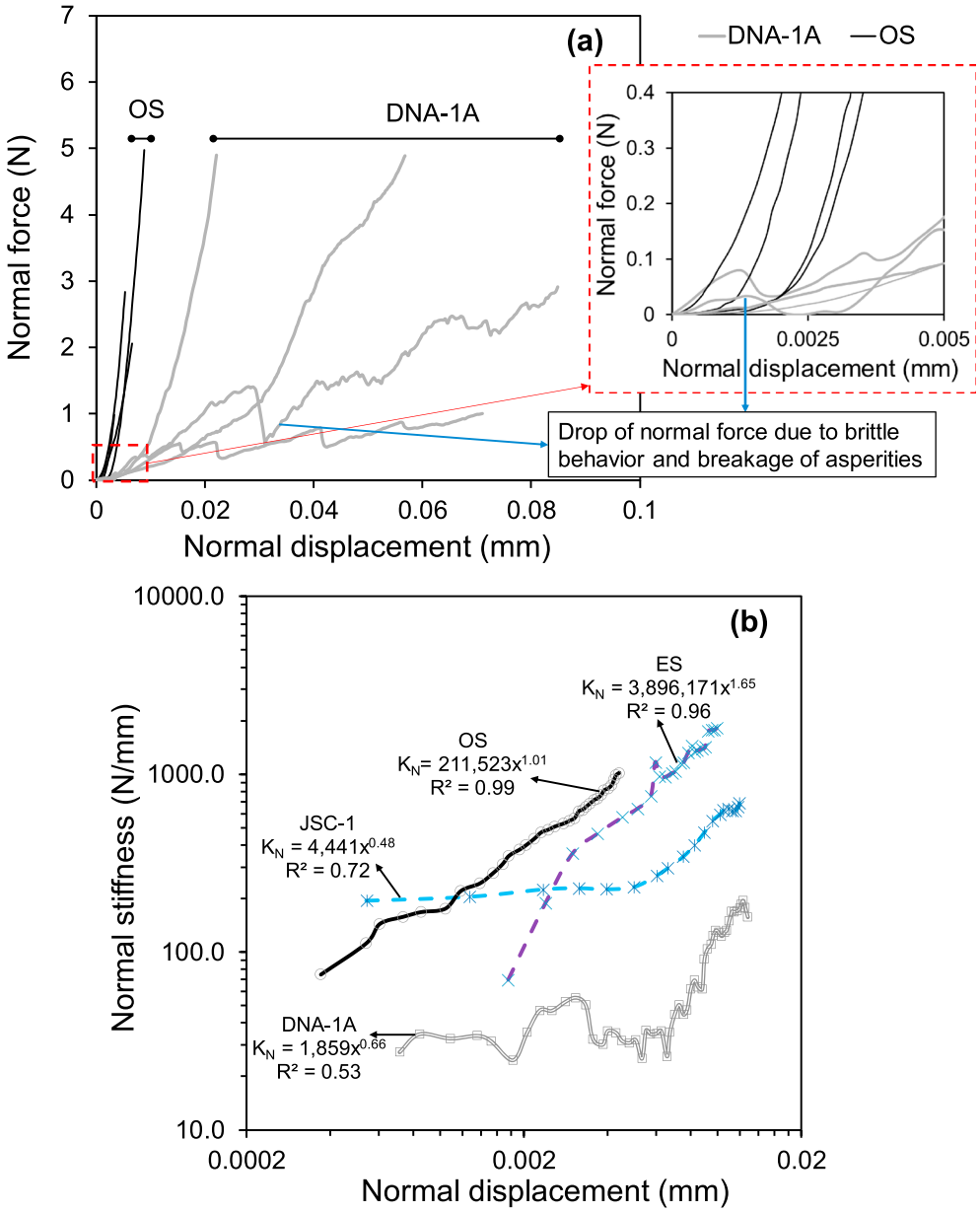

Figure 7. (a) Representative normal force against displacement curves for DNA-1A and Ottawa sand (OS) grains. Highlighted part showing greater initial soft displacements of DNA-1A grains when compared to Ottawa sand grains. (b) Representative normal stiffness against displacement behavior of DNA-1A and Ottawa sand (OS) grains in comparison with JSC-1 simulant (after Cole & Peters, 2008) and Eglin sand (ES; after Nardelli et al., 2017).

5.1.2. Theoretical Fitting

Fitting to the experimental normal force–displacement curves was applied using the models proposed by Hertz (1882) and Yimsiri and Soga (2000) (referred as Y&S) and a representative case for Ottawa sand is shown in Figure 8a. In Figure 8b, the data from Figure 8a were reproduced in terms of normal stiffness against normal displacement. For the fitting, the values of Poisson's ratio and radius of the Ottawa sand grains were taken as 0.1 and 0.35 mm, respectively. As highlighted earlier, the Hertz theory of contact fits the experimental curves reasonably well after the initial regime of plastic displacements (0.7 μm for the example in Figure 8a) and Young's modulus for the best fit based on visual observation was obtained as 39 GPa. Applying the Y&S model, as shown in Figure 8a, the theoretical curve fitted the experimental

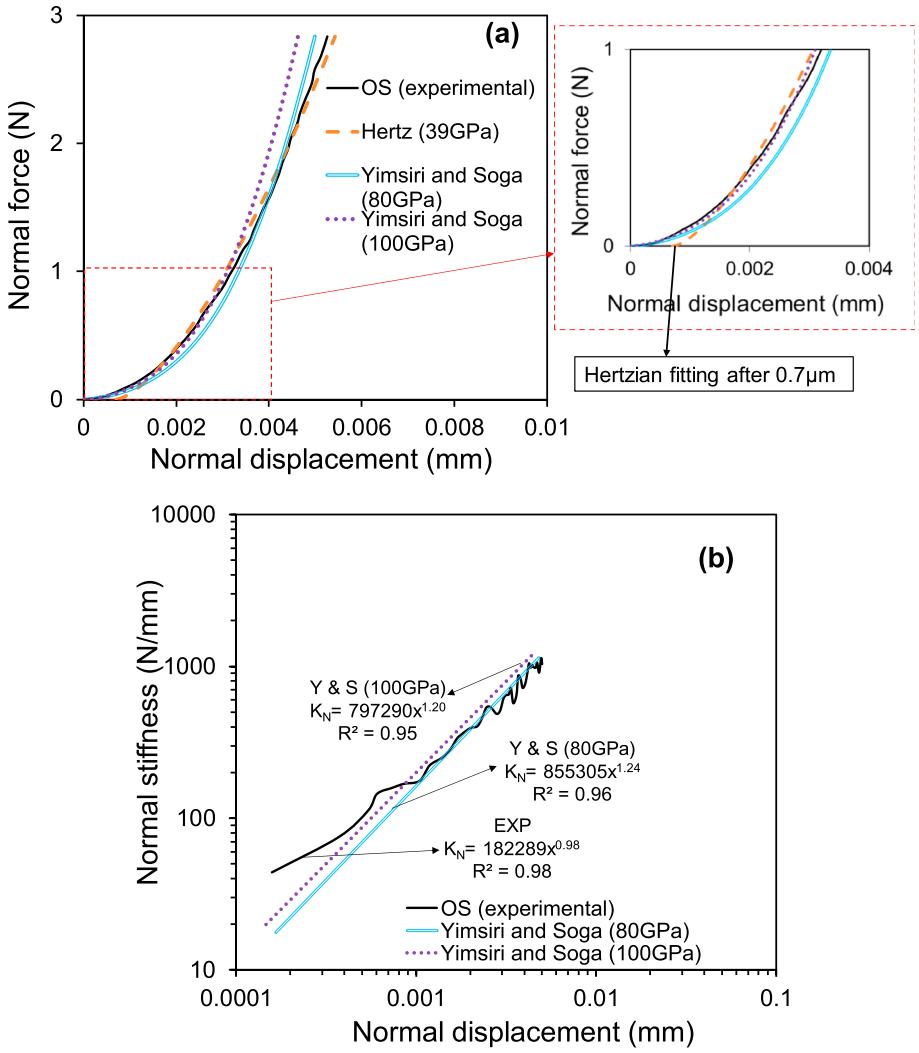

Figure 8. (a) Theoretical fitting for experimental normal force against displacement response of Ottawa sand (OS) grain pair highlighting differences among different fitting techniques. (b) Normal stiffness against displacement response of Ottawa sand (OS) grains from experiment and theoretical models.

data reasonably well from the initial regime of plastic displacements up to about 1 N of normal force when Young's modulus of 100 GPa was used as a fitting parameter. However, using a fitting value of 100 GPa for Young's modulus, the theoretical curve showed a stiffer response beyond about 1 N compared with the experimental curve. This behavior was clearly visible in the data of Figures 8a and 8b. When the value of Young's modulus equaled to 80 GPa (Figure 8b), the theoretical curve fitted well the experimental curve with some deviation in the initial regime of the data, but with a much better fitting thereafter.

Figure 9a presents theoretical fitting of representative normal force against displacement curves of DNA-1A grains. For the fitting of the experimental data in both normal and tangential directions using the models proposed by Hertz (1882) and Yimsiri and Soga (2000), the values of Poisson's ratio and radius of the DNA-1A grains were taken as 0.3 and 0.8 mm, respectively. A deviation between Hertz contact model and experimental curves was observed at the initial regime of compression which is attributed to the significant plastic displacements observed on DNA-1A at the early stages of the application of the normal force. A comparison between experimental data and Y&S model in terms of normal stiffness against displacement is illustrated in Figure 9b. Despite the fluctuations in the experimental data, the model by Y&S satisfactorily fits the experimental results. It is speculated that the observed differences in the application of the Y&S model

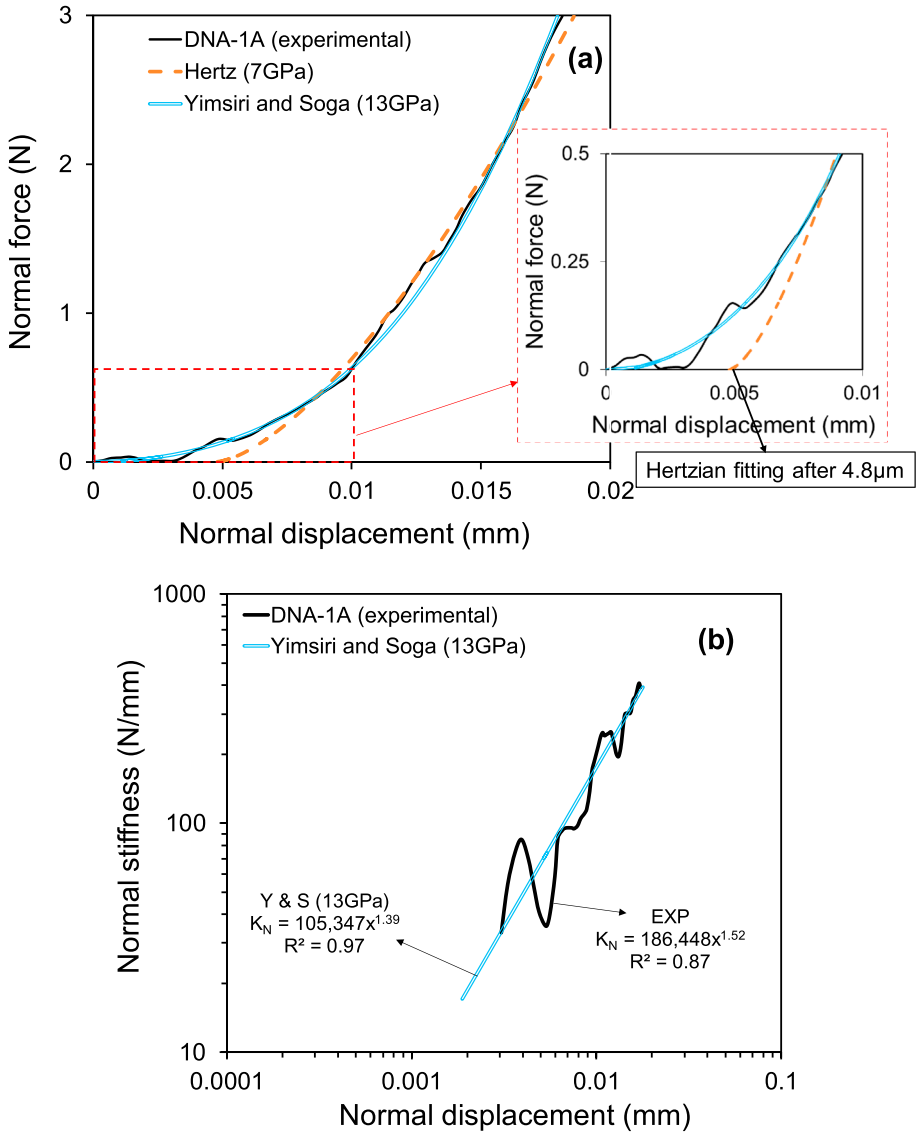

Figure 9. (a) Theoretical fitting for experimental normal force against displacement response of DNA-1A grain pair highlighting differences among different fitting techniques. (b) Normal stiffness against displacement response of DNA-1A grains from experiment and theoretical models.

between Ottawa sand of relatively smooth surfaces and DNA-1A of much rougher surfaces might be due to the smoothening of the surface asperities of Ottawa sand grains at smaller magnitudes of normal force, whereas for DNA-1A, it is hypothesized that debris is created during compression, which is advanced because of the relatively brittle behavior of the asperities. The latter hypothesis is further supported with microscope image observations as it will be discussed in subsequent sections. Hence, the rough surface contact model can mimic the trend of the experimental curve much better for DNA-1A grains when compared with Ottawa sand grains.

Based on the total set of experimental results and corresponding curves plotted using the Hertz contact model, the average value of Young's modulus for DNA-1A and Ottawa sand grains were equal to 5.2 and 48 GPa with a standard deviation of ±3 and ±15 GPa, respectively. Using the rough surface contact model of Yimsiri and Soga (2000), Ottawa sand showed relatively higher values of Young's modulus ranging from 76 to 109 GPa. The average value of Young's modulus for DNA-1A and Ottawa sand grains

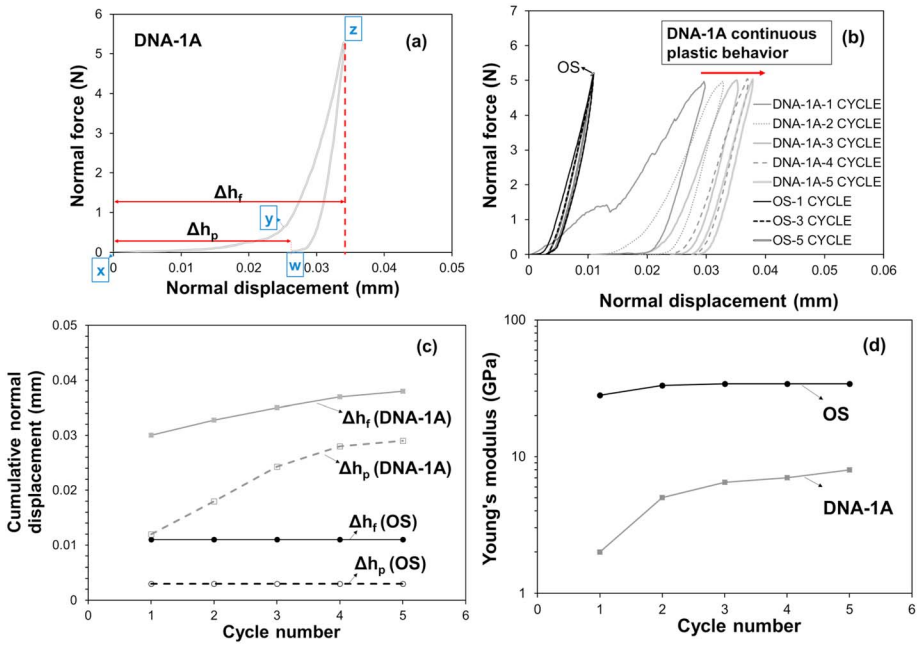

Figure 10. (a) Various stages of loading and unloading curve for DNA-1A highlighting final (Δh_f) and plastic displacement (Δh_p). (b) Cyclic compression behavior of DNA-1A and Ottawa sand (OS) grains where continuous plastic response is observed for DNA-1A. (c) Cumulative final and plastic displacement against cycle number for DNA-1A and Ottawa sand grains (OS). (d) Young's modulus (Hertzian) against cycle number showing continuous increase in Young's modulus with cycle number for DNA-1A and Ottawa sand (OS) grain pairs.

using Y&S model was equal to 11 and 83 GPa with a standard deviation of ±4 and ±17 GPa, respectively. The Young's modulus values of Ottawa sand grains obtained through Y&S model are similar to the value reported by Nardelli and Coop (2018) for LBS grains (E = 94 GPa). For both tested materials, Hertz model cannot fit the initial regime of plastic displacements. Researchers using numerical tools such as DEM may consider the initial plastic displacements while applying the Hertz contact model. However, the rough surface contact model by Yimsiri and Soga (2000) fits the experimental curves reasonably well for Ottawa sand and DNA-1A grains for the entire span of the experimental data without ignoring the initial plastic displacements.

5.1.3. Cyclic Compression

Figures 10a and 10b present the cyclic compression tests conducted on DNA-1A and Ottawa sand pairs of grains. The loading and unloading curve can be divided into three stages (Figure 10a), with stiffness during the initial stages of loading (from point "x" to point "y") being very low due to plastic deformation of surface asperities (below 0.7 N for DNA-1A in Figure 10a). At this point, an increase of stiffness was observed during loading from point y to point "z" reaching final displacement of Δh_f. During the unloading stage (from point z to point "w"), the behavior was stiffer compared with the loading curve (from point x to point z). Some plastic deformation (denoted as Δh_p) was detected which is primarily a reflection of the deformed and/or damaged surface asperities. Figure 10c shows the variation of the cumulative plastic and total displacements against the number of cycles. From Figures 10b and 10c, it was observed that for Ottawa sand grains plastic displacements occurred, predominantly, in the first cycle after which elastic displacements were dominant. However, for DNA-1A grains, a major portion of plastic displacements occurred during the first cycle and this plastic behavior continued in the later cycles as well. This increase in plastic deformations with cycle number is advanced by the high roughness and low stiffness during compression.

The Hertz contact model was fitted to the loading portion of the cyclic compression curves beyond the regime of initial plastic deformations for both materials. The changes in Young's moduli with cycle number are reported in Figure 10d. For the Ottawa sand, an increase in Young's modulus was observed from the first

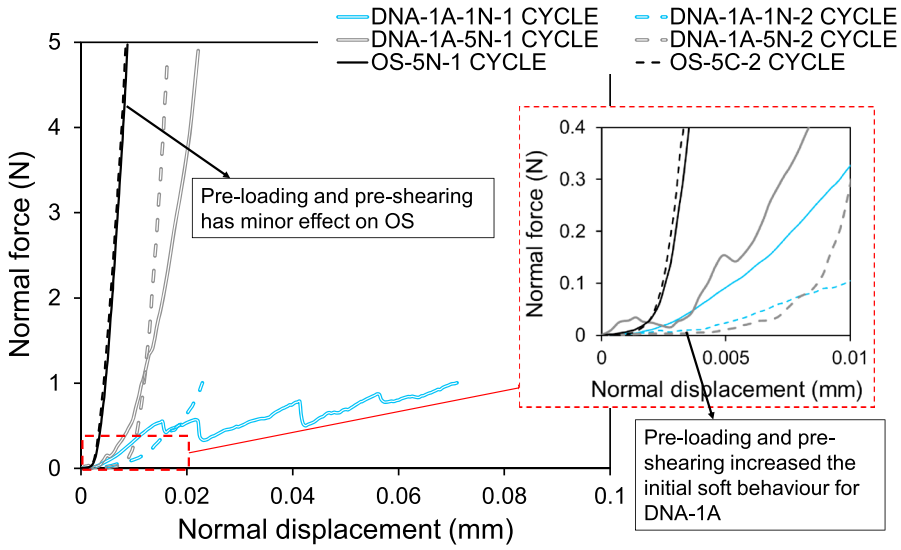

Figure 11. Representative curves showing the effect of preloading and preshearing on the normal compression response of DNA-1A-9, DNA-1A-12, OS-9, and OS-12 pairs of grains. Highlighted portion shows increase in initial soft behavior for DNA-1A in the second compression cycle.

to the second cycle on the order of 25%, after which Young's modulus mostly remained constant, which agrees with previous results on LBS by Sandeep and Senetakis (2018a). However, for the DNA-1A pair of grains, the Young's modulus increased almost 5 times from the first to the second cycle and about 2.5 times from the second to the third cycle while this increase of Young's modulus was observed to be much

Table 3
Summary of the Micromechanical Testing Program

		Tangential force (N)		Interparticle friction	
Code	Normal force (N)	First cycle	Second cycle	First cycle	Second cycle
DNA-1A-1	1	0.50	-	0.50	-
DNA-1A-2	2	0.70	-	0.35	-
DNA-1A-3	3	1.16	-	0.39	-
DNA-1A-4	5	2.55	-	0.51	-
DNA-1A-5	1	0.39	-	0.39	-
DNA-1A-6	2	0.60	-	0.30	-
DNA-1A-7	3	0.90	-	0.30	-
DNA-1A-8	5	1.89	-	0.38	-
DNA-1A-9	1	0.23	0.16	0.23	0.16
DNA-1A-10	2	0.46	0.23	0.23	0.12
DNA-1A-11	3	1.08	0.84	0.43	0.22
DNA-1A-12	5	1.56	1.93	0.31	0.39
OS-1	1	0.12	-	0.12	-
OS-2	2	0.25	-	0.13	-
OS-3	3	0.52	-	0.17	-
OS-4	5	0.49	-	0.10	-
OS-5	1	0.13	-	0.13	-
OS-6	2	0.17	-	0.09	-
OS-7	3	0.33	-	0.11	-
OS-8	5	0.70	-	0.14	-
OS-9	1	0.15	0.16	0.15	0.16
OS-10	2	0.26	0.22	0.13	0.11
OS-11	3	0.20	0.17	0.07	0.06
OS-12	5	0.36	0.23	0.07	0.05

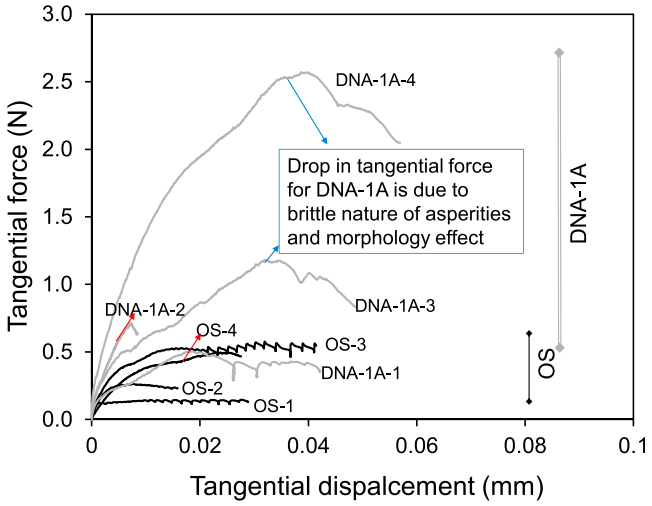

Figure 12. Representative tangential force against displacement curves for DNA-1A and Ottawa sand (OS) grains.

smaller in the subsequent fourth and fifth cycles, till measurable. It is worth noticing that for the soft granules of a weathered tuff from a recent landslide, Sandeep, Todisco, et al. (2018) reported a substantial increase of the Young's modulus from the first to the second cycle of 1 order in magnitude (from about 0.16–0.20 to 1.4–1.7 GPa), but from the second to the third cycle this increase was less than 10% so that for the regolith simulant there is a significant effect of the second cycle of normal loading which was not observed in previous studies in other geological materials.

5.1.4. Effect of Preloading and Preshearing

Figure 11 shows the compression behavior of representative curves of DNA-1A and Ottawa sand grains during the first cycle (virgin compression) and second cycle (reloading of the grains which were previously subjected to compression and shearing). It is observed that during the second cycle, the Ottawa sand grains showed minor changes in the behavior when compared with the virgin compression curve. The DNA-1A pair of grains, which was subjected to reloading in the second cycle, showed a greater initial soft response (4–6 μm) when compared to the virgin compression curve. However, after the initial regime of plastic displacements which were more pronounced in the second cycle, the DNA-1A curves showed a stiffer response in the second cycle compared with the virgin compression and thus reached the imposed normal force at a smaller magnitude of normal displacement. These results, similar to the recent study by Sandeep and Senetakis (2018c), indicate the possible creation of debris due to the coupled influence of preloading and preshearing which resulted in a softer behavior of the initial regime of the second cycle of normal loading after the completion of the first shearing. Because the pure normal load tests did not show a softer initial regime in the second cycle (i.e., cyclic experiments without the application of shearing as shown in Figure 10), it is speculated that the possible creation of debris at the interface is the result of the shearing at the grain contacts.

5.2. Tangential Contact Behavior

5.2.1. Monotonic Shearing

A summary of the micromechanical test results with information on the interparticle coefficient of friction from the shearing tests is given in Table 3. Representative tangential force against displacement curves for DNA-1A and Ottawa sand are given in Figure 12. The tangential force increased nonlinearly with the displacement, showing a subtle decrease in slope until a slip condition or a steady state shearing was observed. Boitnott et al. (1992) showed that during normal loading, the contacts (asperities) are subjected to different magnitude of normal forces and that during shearing sliding develops gradually, where the contacts under low normal forces tend to slide initially. They proposed that this gradual development of sliding at the contact surface contributes to the nonlinearity in the tangential force against displacement relationship. It was observed that the tangential force to reach the steady state or slip displacement (where the slip displacement is defined at the onset of zeroed tangential stiffness) increased with the increase in the applied normal force for both materials, which is in agreement with the recent study by Sandeep and Senetakis (2019). Figure 13 shows representative tangential stiffness degradation curves.

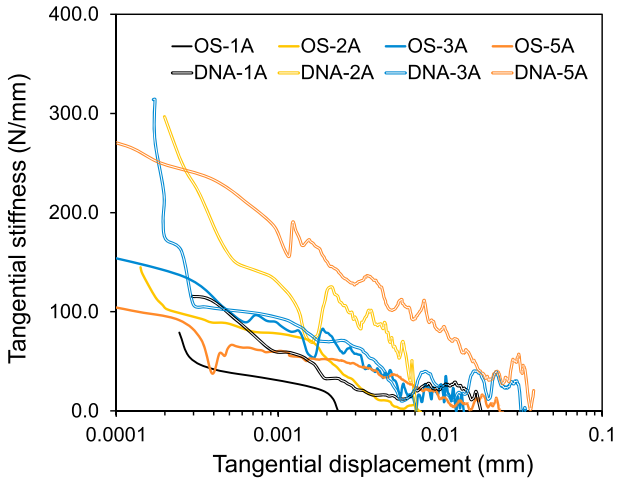

Figure 13. Representative tangential stiffness against displacement behavior for DNA-1A and Ottawa sand (OS) grains.

Based on the results in Figures 12 and 13, a few differences were observed in the tangential contact behavior between DNA-1A and Ottawa sand. For Ottawa sand, stick-slip was observed for most of the specimens after the steady state was reached, which behavior is attributed, predominantly, to the relatively smooth surface of the grains. For DNA-1A grains after reaching the slip displacement, a drop in the

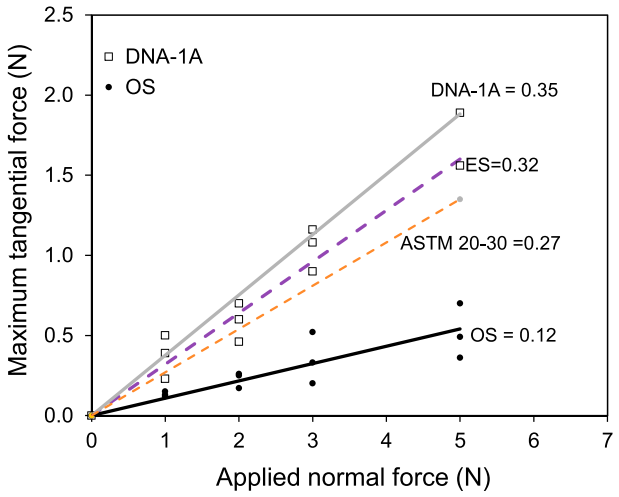

Figure 14. Failure envelopes for DNA-1A and Ottawa sand (OS) grains from the current study in comparison with ASTM 20–30 (after Cole, 2015) and Eglin sand (ES; after Nardelli et al., 2017).

tangential force was observed rather than a clear steady state for most of the specimens. This behavior is speculated to be caused by the rough surface and brittle nature of the contacting asperities for the DNA-1A simulant. The initial tangential stiffness, which is defined in the study at 0.2 μm of tangential displacement (Figure 13), was relatively low in magnitude for the Ottawa sand compared with DNA-1A or reported data on Eglin sand and LBS grains by Nardelli et al. (2017) and Sandeep and Senetakis (2018a, 2018d), respectively. It is noted that Ottawa sand and LBS grains have similar values of Young's modulus and surface roughness. It is speculated that the smaller size of the grains from the Ottawa sand (size of grains between 0.5 and 0.8 mm) compared with LBS grains (average size of 2.0 mm) might have contributed to these lower values of initial tangential stiffness for the Ottawa sand. A previous work by Biegel et al. (1992) showed that the stiffness depends on the roughness and that smooth surfaces tend to have equal or higher tangential stiffness compared to rough surfaces. Comparing DNA-1A and LBS, which materials have very similar size of grains, the initial tangential stiffness is higher for LBS, which material has grains with much smoother surfaces compared with DNA-1A simulant.

In the range of small normal forces, between 1 and 3 N (Figures 12 and 13), it was observed that the DNA-1A pairs of grains had greater slip displacements compared with Ottawa sand specimens. Slip displacement generally depends on grain size and contact area. Previous studies (Olsson & Larsson, 2014; Sandeep & Senetakis, 2019) showed that Young's modulus, surface roughness, and magnitude of normal force also contribute to the slip displacement. These parameters also affect the contact area. Additionally, earlier works (Biegel et al., 1992; Dieterich, 1979; Linker & Dieterich, 1992; Sandeep & Senetakis, 2018a, 2019; Sandeep, Todisco, et al., 2018) showed that the slip displacement increases with the increase in the applied normal force and surface roughness so that the high roughness of the DNA-1A simulant seems to have contributed to these observed trends.

The value of the interparticle friction at the steady state sliding or at the point, beyond which a drop of the force is noticed, is calculated as the ratio of the tangential force (corresponding to a maximum or a steady

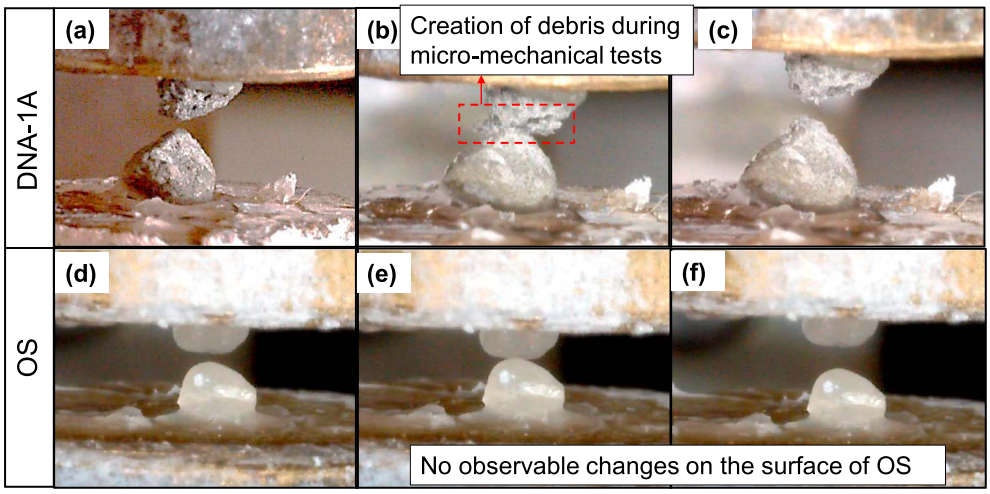

Figure 15. Images of DNA-1A and Ottawa sand (OS) grains (a and d) before testing, (b and e) during application of normal force, and shearing (c and f) after first cycle of shearing.

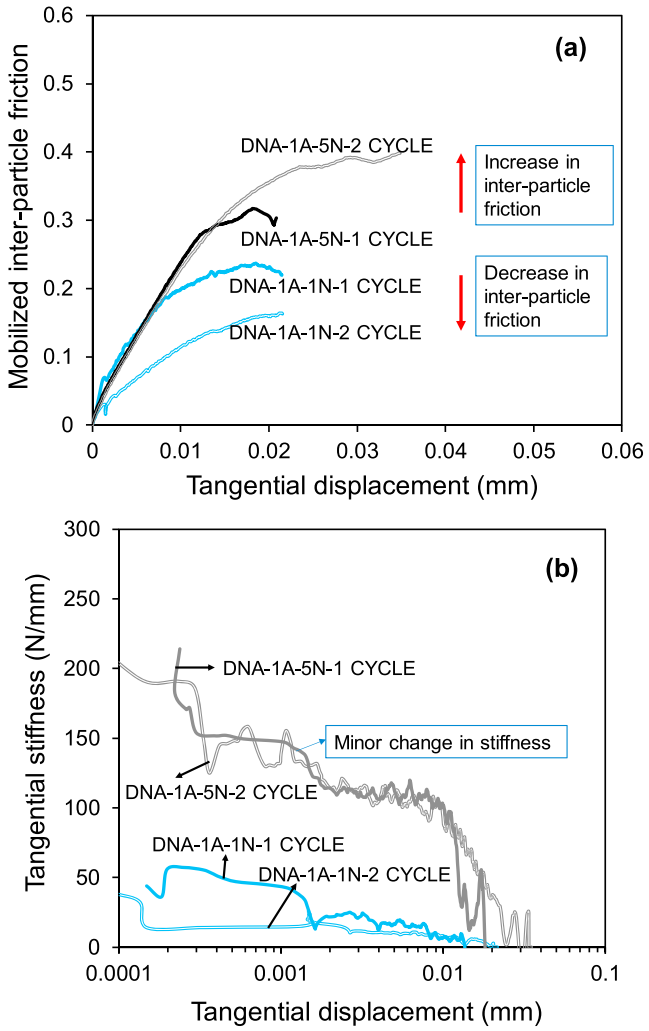

Figure 16. (a) Mobilized interparticle friction against displacement curves for DNA-1A-(9 and 12) grain pairs during first and second cycles of shearing at 1 and 5 N of normal force. (b) Tangential stiffness against displacement curves for DNA-1A-(9 and 12) grain pairs during first and second cycles of shearing at 1 and 5 N of normal force.

state value) to the applied normal force. The failure envelopes of the tested materials along with ASTM 20-30 sand (Cole, 2015) and Eglin sand (denoted as ES; after Nardelli et al., 2017) are presented in Figure 14. Within the scatter of the data, the average interparticle friction (μ) values along with standard deviations for DNA-1A and Ottawa sand grains are 0.36 ± 0.09 and 0.12 ± 0.03, respectively, where the average value of μ corresponds to the slope of the envelope in the maximum tangential force–applied normal force plane (Figure 14). It is concluded that the interparticle friction of DNA-1A simulant is higher than that of other materials, which is, predominantly, attributed to the high surface roughness and low values of Young's modulus for the DNA-1A simulant. For completely decomposed granite, which material has similar surface roughness and Young's modulus with DNA-1A, Sandeep and Senetakis (2018b) reported similar high values of interparticle friction (average $\mu = 0.35$). The higher average μ value for Eglin sand (after Nardelli et al., 2017) compared with Ottawa sand is attributed, predominantly, to the higher roughness values of that material (average $S_q = 0.59$ μm), since Young's moduli are in close proximity between these materials. Testing quartz sand grains from different geological environments, Sandeep, He, et al. (2018) showed that the interparticle friction for materials of very similar Young's modulus, depends, predominantly, on the surface roughness.

5.2.2. Effect of Preloading and Preshearing

Figure 15 shows representative images of DNA-1A and Ottawa sand grains during the micromechanical tests. Inspection of the figure (Figures 15a–15c) shows that for the DNA-1A grains the behavior is complex and the initial morphology of the grains changed during the micromechanical tests creating debris and thus greater initial plastic displacements in the second compression cycle, which behavior was confirmed by the data in Figure 11. It is worth noticing that the morphology of the grains in terms of shape and surface roughness affects the interparticle contact behavior. In previous works by the authors on quartz sand grains and crushed limestone grains (Sandeep & Senetakis, 2018b, 2018d), we observed effects of surface morphology on micromechanical behavior. In the current study, fairly regular shaped DNA-1A grains were taken for the tests, and debris are created during the tests (Figure 15) due to breakage of surface asperities. However, the degree of debris creation might be different among different pairs of grains. For example, in Figure 11 the normal force–displacement curves in the first cycle were different between DNA-1A-9 (tested at $F_N = 1$ N) and DNA-1A-12 (tested at $F_N = 5$ N). For DNA-1A grains with vesicular surface morphology, it is difficult to attribute these changes to shape alone. The creation of debris changed the surface morphology (soil fabric) at the contacts for DNA-1A grains, which may affect the bulk material's strength and deformation characteristics (after Yimsiri & Soga, 2000).

Figure 16a shows the mobilized interparticle friction against displacement for specimens DNA-1A-9 and DNA-1A-12. As observed in Figure 16a and Table 3, the value of the interparticle friction in the second cycle decreased when the grains were sheared at 1–3 N of normal force, whereas μ increased at 5 N of normal force for DNA-1A grains. However, for Ottawa sand the interparticle friction values decreased from the first to the second cycle independent on the applied normal force. Inspection of the images in Figures 15d–15f shows that the combination of normal and tangential loading did not produce notable changes on the surfaces of Ottawa sand grains, as it was observed for DNA-1A simulant. Previous works on preloading and preshearing effects for quartz grains (Sandeep & Senetakis, 2018a; Senetakis et al., 2013a) reported a decrease in the interparticle friction after the grains were subjected to virgin compression and shearing; this behavior was attributed to the smoothening of surface asperities, which was confirmed by measurements of surface roughness

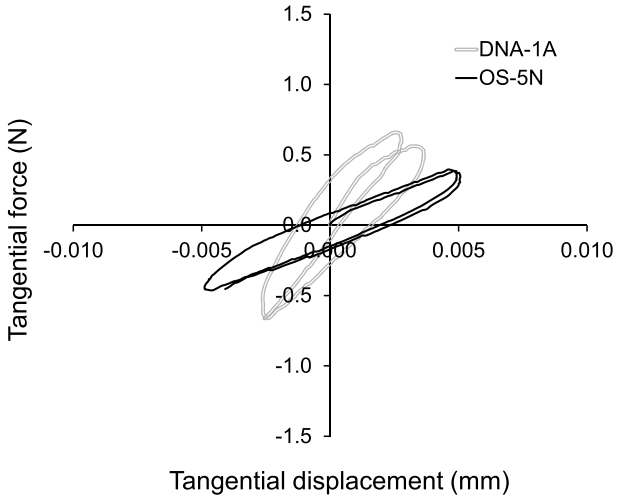

Figure 17. Cyclic shearing of DNA-1A-CS-1 and OS-CS-1 grains for 5-μm displacement amplitude when sheared under 5 N of normal force.

on pairs of LBS grains before and after shearing by Senetakis et al. (2013b). Figure 16b shows the tangential stiffness degradation curves of DNA-1A during the first and second cycles of shearing at 1 and 5 N of normal force. It was observed that during the second cycle of shearing, the tangential stiffness either decreased or changed slightly.

5.2.3. Cyclic Shearing

Figure 17 shows representative cyclic shearing tests conducted on DNA-1A and Ottawa sand pairs of grains at displacement amplitude of 5 μm. The energy loss percentage (ΔE) is calculated based on equation (14), similar to Sandeep and Senetakis (2018a, 2019) from the area of the closed loop (ΔL) over the elastic energy stored (L) from the first part of force displacement prior to reversal of the force (it corresponds to a triangle area). The results from the cyclic tests in terms of energy loss percentage calculated in the second cycle of the experiments are summarized in Table 4.

$$\Delta E = \frac{100\Delta L}{4\pi L} \tag{14}$$

From Table 4, it was observed that for both DNA-1A and Ottawa sand, ΔE increased slightly with the increase in displacement amplitude. For example, for specimens OS-CS-1 and OS-CS-2 from the Ottawa sand tested at 5 and 10 μm of displacement amplitude, ΔE equaled 10% and 13%, respectively. Sandeep, Todisco, et al. (2018) observed a similar increase in energy losses with displacement amplitude for decomposed volcanic granules. However, the energy loss percentage at 10 μm of displacement amplitude for both materials (DNA-1A and Ottawa sand) is less in magnitude than that of LBS grains, for which material, Sandeep and Senetakis (2018a) reported ΔE values on the order of 30–40%. The range of slip displacement values for Ottawa sand grains and LBS grains during shearing were about 15–30 and 4–8 μm, respectively. The higher values of slip displacement and lower values of ΔE for Ottawa sand grains when compared with LBS grains are possibly due to small grain size of Ottawa sand. The observed ΔE values during cyclic shearing for DNA-1A grains are in close proximity to the reported results for decomposed volcanic grains reported by Sandeep, Todisco, et al. (2018) ($\Delta E = 8\%$ and 22% at 5 and 10 μm of displacement amplitude at $F_N = 1$ N). These similarities in the cyclic behavior of DNA-1A simulant and decomposed volcanic grains are attributed, partly, to the nearly similar range of slip displacement values of about 20 to 50 μm during shearing observed for DNA-1A at $F_N = 5$ N and decomposed volcanic grains at $F_N = 1$ N. It is understood that the energy losses during cyclic shearing are governed majorly by the slip displacement and displacement amplitude. Similar observations were also reported by Wang et al. (2018) using finite element analysis for mechanical joints. They showed that the energy losses increase with the increase in displacement amplitude and the decrease in slip displacement.

5.2.4. Theoretical Fitting

Theoretical curves were plotted using Mindlin and Deresiewicz (MD) and Dahl's models for the experimental tangential force against displacement curves for Ottawa sand and DNA-1A specimens. Representative results of this fitting are given in Figure 18. The theoretical curve as shown in Figure 18 revealed a wide gap between MD model and the experimental tangential curves for both material types. Previous works (Nardelli et al., 2017; Sandeep, He, et al., 2018; Sandeep & Senetakis, 2018d, 2019) reported, similarly, mismatch between MD model and experimental results on a broad range of geological materials, when the MD model is used with its originally proposed power of 1/3 (equation (10)). They also reported that differences between MD model and experimental curve can be reduced to some extent by considering initial tangential stiffness derived from experiment rather than from equation (9). In general, the MD model predicts much greater values of initial tangential stiffness (equation (9)) as well as faster degradation

Table 4
Summary of Cyclic Shearing Tests Conducted on DNA-1A and Ottawa Sand (OS)

Code	Normal force (N)	Displacement amplitude (mm)	Energy loss (%)
DNA-1A-CS-1	5	0.005	11
DNA-1A-CS-2	5	0.01	20
OS-CS-1	5	0.005	10
OS-CS-2	5	0.01	13

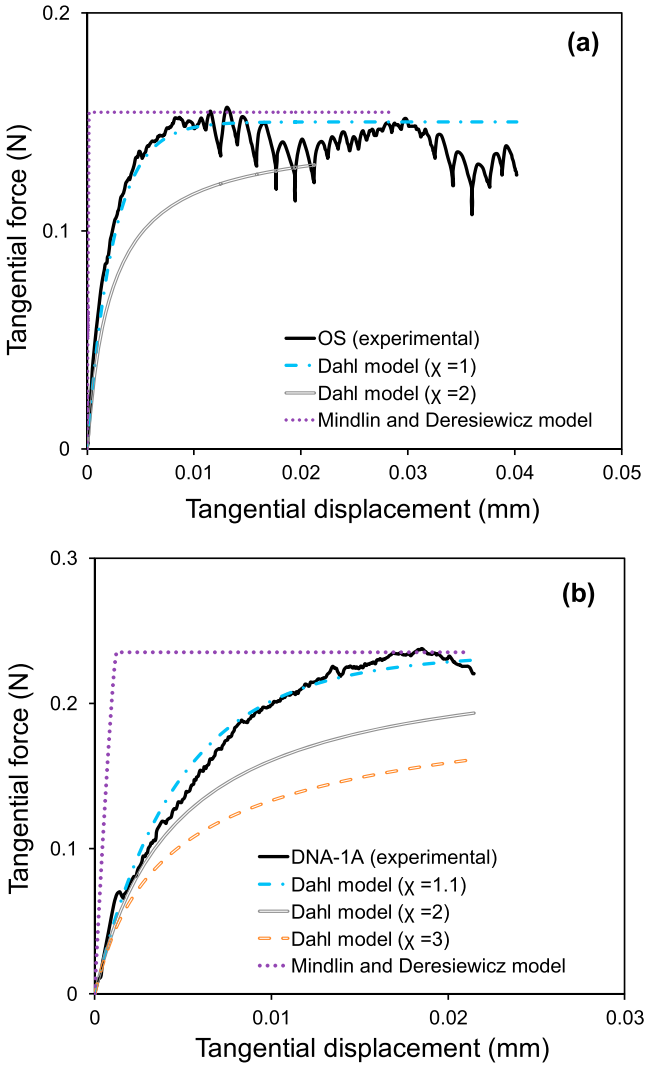

Figure 18. (a) Fitting of OS-9 ($F_N = 1$ N) experimental curve with theoretical Mindlin-Deresiewicz and Dahl's models. (b) Fitting of DNA-1A-9 ($F_N = 1$ N) experimental curve with theoretical Mindlin-Deresiewicz and Dahl's models.

of the tangential stiffness–displacement curves compared with the observed behavior on real sand grain contacts and adjustments of the model are needed to provide a better fitting (Sandeep & Senetakis, 2019).

Aside from the MD theoretical model, Dahl's model was also fitted to the experimental curves using different values for the parameter χ. Dahl's model gives flexibility of choosing the parameters, and therefore, it can be, potentially, of greater interest to researchers to model the nonlinear hysteresis behavior of grain contacts. The initial tangential stiffness values (at 0.2 μm of tangential stiffness) obtained from respective experiments were used for the fitting. As shown in Figures 18a and 18b, a reasonably good fitting was observed for DNA-1A and Ottawa sand grains ($F_N = 1$ N) with Dahl's model when the value of χ was around 1. However, Dahl's model could not capture the observed stick-slip behavior for Ottawa sand or the sudden drop in the tangential force at the onset of slip displacement as it was observed for DNA-1A simulant. For specimen DNA-1A-CS-2 ($F_N = 5$ N) which was subjected to cyclic shearing, theoretical curve using Dahl's model is shown in Figure 19. It was observed that for a value of χ equal to 2, the Dahl's model appeared to fit well the experimental cyclic curves, apart from a small mismatch at the edges of the loops. Dahl's model was also attempted to fit into few other experimental tangential force against displacement curves for both DNA-1A and Ottawa sand. Based on the fitting of theoretical models to the experimental tangential force against displacement curves, it is concluded that the value of shape parameter χ can range, in general, between 1 and 2 for a reasonable fitting of the experimental data for the materials included in the present study. It is recommended that in DEM analyses, when researchers apply the Dahl's model for the tangential force–displacement relationship, the experimentally obtained interparticle friction and stiffness values (Figures 12–14 and Table 3) and the value of χ in the range of 1–2 could be implemented.

In the earlier studies by the authors (Sandeep & Senetakis, 2018a), we observed some deviations between experimental data and theoretical models (Hertz and Mindlin-Dereswiecz) even after considering local radius (or local shape) of the grains. These models were proposed to solve problems related to engineering materials, such as steel, while their application into the study of geological materials which have contacts of brittle or elastic-plastic to brittle in nature needs a systematic assessment with the experimental data to check their predictive capabilities. In this work, we are highlighting the need to consider realistic contact laws, such as Yimsiri and Soga for more accurate modeling.

The observed trends for the grains in terms of normal and tangential loading behavior are at the microscale, in specific testing two grains at their contact. However, for a bulk of grains which is a complex system, apart from the interparticle friction (as well as tangential stiffness and normal contact behavior), other parameters/mechanisms also affect the behavior of the bulk, for example, shape, rolling, possible crushing, and redistribution of grains (rearrangement) and grain contacts. All these macroscopic aspects can be investigated, partly, in element tests, and also, DEM can provide very useful information of the bulk behavior with microscopic observations. An important motivation behind our research was to study the mechanical behavior of DNA-1A and Ottawa sand at the grain scale (i.e., grain-contact response), which can be thereafter used and linked in DEM studies, or explain qualitatively observations from element tests. In other words, the grain contact study comes to be a very fundamental step in understanding the mechanical behavior of granular materials and it is in a sense supportive to macroscale and multiscale studies.

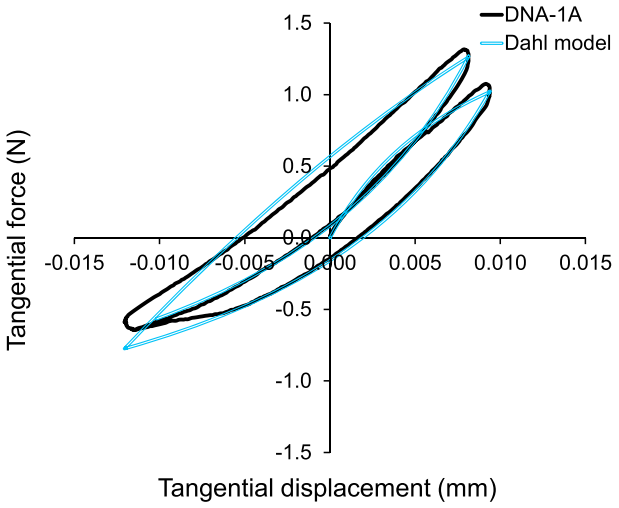

Figure 19. Fitting of DNA-1A-CS-2 cyclic tangential force against displacement curve ($F_N = 5$ N) with Dahl's model ($\chi = 2$).

6. Conclusions

The interparticle contact behavior of DNA-1A simulant and Ottawa sand grains was investigated in this study using a custom-built micromechanical loading apparatus. Material characterization was carried out using several techniques. Based on scanning electron microscope images, it was observed that the DNA-1A grains have vesicular texture and irregular shape, whereas the Ottawa sand grains are relatively regular in shape with smooth surfaces. The surface roughness and hardness of representative sets of grains were obtained using an optical surface profiler and a microhardness tester. The average surface roughness of DNA-1A and Ottawa sand grains were found to be equal to 1,476 ± 379 and 204 ± 42 nm, respectively. The high surface roughness of DNA-1A is primarily due to grinding and crunching of the material during preparation. The Martens hardness of DNA-1A (0.32 GPa) was found to be much lower than that of Ottawa sand (5.8 GPa) which is, predominantly, because of the differences in composition and surface morphology between the two materials.

Based on the micromechanical interparticle loading tests, both materials showed nonlinear behavior during normal compression and shearing. The DNA-1A grains had very low values of normal stiffness and greater initial plastic displacements during compression compared to Ottawa sand grains. The initial plastic displacements during virgin normal loading ranged between 1.1–5.1 and 0.2–0.8 μm for DNA-1A and Ottawa sand grains, respectively. From the cyclic normal loading tests, it was observed that the compression curves showed a stiffer response during the unloading phase for both material types. For DNA-1A, the cumulative plastic displacements continued to increase with the increase in the number of cycles. For Ottawa sand grains a major plastic displacement occurred only during the virgin compression cycle which was followed by predominantly elastic response in the subsequent cycles. From previous works on other geological materials during cyclic compression, it was observed that the apparent value of Young's modulus increased, predominantly, from the first to the second cycle and no significant changes were observed in the subsequent cycles. However, DNA-1A simulant showed to have a significant increase of Young's modulus of about 2.5 times between the second and third compression cycles. Based on these findings we observed that the vesicular texture of the DNA-1A simulant may play an important role in the accumulation of plastic strains beyond the first loading cycle, which behavior was not evident on weathered soils/rocks studied before. These outcomes imply that researchers in implementing realistic behavior of lunar regolith in computer simulations should take into account the important influence of the number of cycles, beyond the virgin compression, in the representation of the normal load–displacement behavior.

From the tangential shearing tests, the DNA-1A specimens had a drop of the tangential force beyond the onset of slip displacement, while for Ottawa sand grains, stick-slip behavior was observed for most pairs of grains. The initial tangential stiffness (defined at 0.2 μm of tangential displacement) was relatively low in magnitude for Ottawa sand compared with DNA-1A grains; this behavior was attributed, partly, to the small size of the grains tested from Ottawa sand. The average values of the interparticle coefficient of friction for DNA-1A and Ottawa sand were equal to 0.36 ± 0.09 and 0.12 ± 0.03, respectively. Based on the present study as well as previously published works, we conclude that the high interparticle friction values of DNA-1A are mainly due to the softer response and high surface roughness of the grains.

During preloading and preshearing tests, the DNA-1A grains showed greater initial plastic displacement and stiffer response during the reloading compared to the virgin normal loading, but for Ottawa sand, preloading and preshearing effects were almost negligible for the range of normal loads covered in the study. Based on observations from microscopic images, it was observed that the higher amount of debris created at the surfaces of the DNA-1A grains might have played an important role on the frictional behavior of the simulant. In this regard, the comparison between DNA-1A, of low hardness, and Ottawa sand, of much higher hardness, leads to the conclusion that preloading and preshearing effects are related, predominantly, with the hardness and to some extent with the morphological characteristics of the grains. For both materials, in

the majority of the tests, the interparticle friction values reduced from the first shearing to the second shearing which is speculated to be because of the smoothening of surface asperities. From the cyclic shearing tests, it was observed that the energy losses increased with the increase in displacement amplitude and the decrease in slip displacement. Therefore, it is concluded that the amount of energy losses at the particle contacts during shearing is related, predominantly, with the roughness and elastic characteristics of the grains.

In the normal direction, the models proposed by Hertz and Yimsiri-Soga were used to fit the experimental data. It was observed that while the theoretical curves plotted using Hertz contact theory could not capture the initial regime of plastic displacements observed in the normal force–displacement curves. The model by Yimsiri-Soga could better fit the experimental data over the entire span (even in the initial stages); this is due to considering the effect of surface roughness. In the tangential direction, Mindlin-Deresiewicz and Dahl's models were applied to fit the experimental curves. Due to the flexibility of Dahl's model in choosing the initial tangential stiffness and the rate of stiffness degradation, a good match with experimental data was observed when the value of χ (fitting parameter in Dahl's model) between about 1 and 2 was used. From the fact that Dahl's model fits the experimental data better than Mindlin-Deresiewicz model, we conclude that the tangential stiffness of the geological materials in the present study degrades slower than the predicted values by Mindlin-Deresiewicz model (power = 1/3). It is therefore suggested that the application of Dahl's model gives greater flexibility to a researcher to incorporate a realistic tangential contact model in a DEM simulation since Dahl's model uses flexible parameters in its expression.

Numerical modeling of the behavior of lunar regolith simulant at low mean stress levels or interactions of lunar regolith with rover vehicles requires grain-scale parameters such as interparticle friction as well as normal and tangential contact stiffnesses which were obtained experimentally in the present study. Additionally, in this study, the effect of loading history on the micromechanical behavior of the lunar simulant was presented in terms of repeated shearing and cyclic loading. These tests provide an assessment of changes in plastic displacements, Young's modulus, and interparticle friction. It is worth noticing that the contact behavior of lunar regolith grains is highly nonlinear and the application of Yimsiri and Soga (2000) and Dahl (1976) models in the normal and tangential directions, respectively, along with parameters obtained from this study (for example, Young's modulus, parameter χ, interparticle friction, normal and tangential stiffness) can be used for realistic simulations of granular assemblies. This can be particularly useful in theoretical analyses of lunar regolith, but the results from the study can also have a broader range of application in different material types.

Acknowledgments
The authors appreciate the constructive comments and suggestions made by the reviewers to improve the quality of the manuscript. The work presented in the article was fully supported by a grant from the Research Grants Council of the Hong Kong Special Administrative Region, China, project 9042491 (CityU 11206617), and a grant (RICAUTOFINCAFAROFRANCESCO) from the Department of Civil, Environmental, Land, Building Engineering and Chemistry, Politecnico di Bari, Bari, Italy. The data of this study are available in the "Supporting data" excel file as supporting information, and additionally, a supplementary doc file provides description of the excel file data sheets for easy access by the reader to the whole data set of micromechanics experiments. These supplementary files accompany the manuscript on the online submission system.

References

Alshibli, K. A., & Hasan, A. (2009). Strength properties of JSC-1A lunar regolith simulant. *Journal of Geotechnical and Geoenvironmental Engineering*, *135*(5), 673–679.

Balevicius, R., & Mroz, Z. (2018). Modeling of combined slip and finite sliding at spherical grain contacts. *Granular Matter*, *20*(1), 10.

Biegel, R. L., Wang, W., Scholz, C. H., Boitnott, G. N., & Yoshioka, N. (1992). Micromechanics of rock friction 1. Effects of surface roughness on initial friction and slip hardening in westerly granite. *Journal of Geophysical Research*, *97*(B6), 8951–8964. https://doi.org/10.1029/92JB00042

Boitnott, G. N., Biegel, R. L., Scholz, C. H., Yoshioka, N., & Wang, W. (1992). Micromechanics of rock friction 2: Quantitative modeling of initial friction with contact theory. *Journal of Geophysical Research*, *97*(B6), 8965–8978. https://doi.org/10.1029/92JB00019

Cafaro, F., Miticocchio, E., & Marzulli, V. (2018). Remarks on the sources of error in the modelling of lunar geotechnical structures. *Studia Geotechnica et Mechanica*, *40*(2), 133–139. https://doi.org/10.2478/sgem-2018-0012.

Carrier, W. D. III (2003). Particle size distribution of lunar soil. *Journal of Geotechnical and Geoenvironmental Engineering*, *129*(10), 956–959.

Cattaneo, C. (1938). Sul contatto di due corpi elastici: Distribuzione locale degli sforzi, vol. *27*. *Rendiconti dell'Accademia Nazionale dei Lincei*, pp. 342–348 (in Italian).

Cavarretta, I., Coop, M., & O'Sullivan, C. (2010). The Influence of particle characteristics on the behavior of coarse grained soils. *Geotechnique*, *60*(6), 413–423.

Cesaretti, G., Dini, E., de Kestelier, X., Colla, V., & Pambaguian, L. (2014). Building components for an outpost on the lunar soil by means of a novel 3D printing technology. *Acta Astronautica*, *93*, 430–450.

Cole, D. M. (2015). Laboratory observations of frictional sliding of individual contacts in geologic materials. *Granular Matter*, *17*(1), 95–110.

Cole, D. M., & Peters, J. F. (2008). Grain-scale mechanics of geologic materials and lunar simulants under normal loading. *Granular Matter*, *10*(3), 171.

Conroy, M., & Mansfield, D. (2008). Scanning interferometry: Measuring microscale devices. *Nature Photonics*, *2*(11), 661.

Costes N. C., Mitchell J. K. (1970). Apollo 11: Soil mechanics investigation. Proc., Apollo 11 Lunar Science Conf., Vol. 3, Lunar and Planetary Institute (LPI) and NASA Johnson Space Center (JSC), Houston, 2025–2044.

Cundall, P. A., & Strack, O. D. (1979). A discrete numerical model for granular assemblies. *Geotechnique*, *29*(1), 47–65.

Dahl, P. R. (1976). Solid friction damping of mechanical vibrations. *AIAA Journal*, *14*(12), 1675–1682.

Daphalapurkar, N. P., Wang, F., Fu, B., Lu, H., & Komanduri, R. (2011). Determination of mechanical properties of sand grains by nanoindentation. *Experimental Mechanics*, *51*(5), 719–728.

De Oliveira, R. R. L., Albuquerque, D. A. C., Cruz, T. G. S., Yamaji, F. M., & Leite, F. L. (2012). Measurement of the nanoscale roughness by atomic force microscopy: basic principles and applications. In *Atomic force microscopy-imaging, measuring and manipulating surfaces at the atomic scale* (pp. 147–175). Rijeka, Croatia: InTech.

Dieterich, J. H. (1979). Modeling of rock friction: 1. Experimental results and constitutive equations. *Journal of Geophysical Research*, *84*(B5), 2161–2168. https://doi.org/10.1029/JB084iB05p02161

Erdogan, S. T., Forster, A. M., Stutzman, P. E., & Garboczi, E. J. (2017). Particle-based characterization of Ottawa sand: Shape, size, mineralogy, and elastic moduli. *Cement and Concrete Composites*, *83*, 36–44.

Gadelmawla, E. S., Koura, M. M., Maksoud, T. M. A., Elewa, I. M., & Soliman, H. H. (2002). Roughness parameters. *Journal of Materials Processing Technology*, *123*(1), 133–145.

Ghosh, S., Rai, C. S., Sondergeld, C. H., & Larese, R. E. (2014). Experimental investigation of proppant diagenesis. In SPE/CSUR Unconventional Resources Conference–Canada. Society of Petroleum Engineers.

Griepentrog, M., Ullner, C., & Duck, A. (2002). Instrumented indentation test for hardness and materials parameter from millinewtons to kilonewtons. *VDI Berichte*, *1685*, 105–112.

Guo, N., & Zhao, J. (2016). Multiscale insights into classical geomechanics problems. *International Journal for Numerical and Analytical Methods in Geomechanics*, *40*(3), 367–390.

Hasan, A., & Alshibli, K. A. (2010). Discrete element modeling of strength properties of Johnson Space Center (JSC-1A) lunar regolith simulant. *Journal of Aerospace Engineering*, *23*(3), 157–165.

Hertz, H. (1882). Ueber die Verdunstung der Flüssigkeiten, insbesondere des Quecksilbers, im luftleeren Raume. *Annalen der Physik*, *253*(10), 177–193.

Hill, E., Mellin, M. J., Deane, B., Liu, Y., & Taylor, L. A. (2007). Apollo sample 70051 and high- and low-Ti lunar soil simulants MLS-1A and JSC-1A: Implications for future lunar exploration. *Journal of Geophysical Research*, *112*, E02006. https://doi.org/10.1029/2006JE002767

Horanyi, M., Walch, B., Robertson, S., & Alexander, D. (1998). Electrostatic charging properties of Apollo 17 lunar dust. *Journal of Geophysical Research*, *103*(E4), 8575–8580. https://doi.org/10.1029/98JE00486

Hu, M., O'Sullivan, C., Jardine, R. R., & Jiang, M. (2010). Stress-induced anisotropy in sand under cyclic loading. *Granular Matter*, *12*(5), 469–476.

Huang, X., Hanley, K. J., O'Sullivan, C., & Kwok, C. Y. (2014). Exploring the influence of interparticle friction on critical state behaviour using DEM. *International Journal for Numerical and Analytical Methods in Geomechanics*, *38*(12), 1276–1297.

Iverson, R. M., Reid, M. E., Logan, M., LaHusen, R. G., Godt, J. W., & Griswold, J. P. (2011). Positive feedback and momentum growth during debris-flow entrainment of wet bed sediment. *Nature Geoscience*, *4*(2), 116.

Jiang, M., Shen, Z., & Utili, S. (2016). DEM modeling of cantilever retaining excavations: Implications for lunar constructions. *Engineering Computations*, *33*(2), 366–394.

Johnson, K. L. (1985). *Contact mechanics*. Cambridge: Cambridge University Press.

Kermani, E., Qiu, T., & Li, T. (2015). Simulation of collapse of granular columns using the discrete element method. *International Journal of Geomechanics*, *15*(6), 04015004.

Knuth, M. A., Johnson, J. B., Hopkins, M. A., Sullivan, R. J., & Moore, J. M. (2012). Discrete element modeling of a Mars Exploration Rover wheel in granular material. *Journal of Terramechanics*, *49*(1), 27–36.

Krid, M., Benamar, F., & Lenain, R. (2017). A new explicit dynamic path tracking controller using generalized predictive control. *International Journal of Control, Automation and Systems*, *15*(1), 303–314.

Li, W., Huang, Y., Cui, Y., Dong, S., & Wang, J. (2010). Trafficability analysis of lunar mare terrain by means of the discrete element method for wheeled rover locomotion. *Journal of Terramechanics*, *47*(3), 161–172.

Linker, M. F., & Dieterich, J. H. (1992). Effects of variable normal stress on rock friction: Observations and constitutive equations. *Journal of Geophysical Research*, *97*(B4), 4923–4940. https://doi.org/10.1029/92JB00017

Markandeya Raju, P., & Pranathi, S. (2012). Lunarcrete: A review. Proceedings of AARCV 2012 - International Conference on Advances in Architecture and Civil Engineering, 21st – 23rd June 2012 Paper ID AR84AS, Vol.2, pp. 886–891.

Marzulli, V., & Cafaro, F. (2019). Geotechnical properties of uncompacted DNA-1A lunar simulant. *Journal of Aerospace Engineering*, *32*(2). https://doi.org/10.1061/(ASCE)AS.1943-5525.0000983

McKay, D. S., Carter, J. L., Boles, W. W., Allen, C. C., & Allton, J. H. (1994). JSC-1: A new lunar soil simulant. *Engineering, Construction, and Operations in space IV*, *2*, 857–866.

Meurisse, A., Beltzung, J. C., Kolbe, M., Cowley, A., & Sperl, M. (2017). Influence of mineral composition on sintering lunar regolith. *Journal of Aerospace Engineering*, *30*(4), 04017014.

Mindlin, R. D. (1949). Compliance of elastic bodies in contact. *Journal of Applied Mechanics*, *16*, 259–268.

Mindlin, R. D., & Deresiewicz, H. (1953). Elastic spheres in contact under varying oblique forces. *Journal of Applied Mechanics*, *20*, 327–344.

Nakashima, H., Fujii, H., Oida, A., Momozu, M., Kanamori, H., Aoki, S., et al. (2010). Discrete element method analysis of single wheel performance for a small lunar rover on sloped terrain. *Journal of Terramechanics*, *47*(5), 307–321.

Nakashima, H., Shioji, Y., Kobayashi, T., Aoki, S., Shimizu, H., Miyasaka, J., & Ohdoi, K. (2011). Determining the angle of repose of sand under low-gravity conditions using discrete element method. *Journal of Terramechanics*, *48*(1), 17–26.

Nardelli, V., & Coop, M. R. (2018). The experimental contact behaviour of natural sands: normal and tangential loading. *Géotechnique*. https://doi.org/10.1680/jgeot.17.P.167

Nardelli, V., Coop, M. R., Andrade, J. E., & Paccagnella, F. (2017). An experimental investigation of the micromechanics of Eglin sand. *Powder Technology*, *312*, 166–174.

NASA (2018). https://lunar.gsfc.nasa.gov/lessonkit/Total.pdf

Olsson, E., & Larsson, P. L. (2014). On the tangential contact behavior at elastic–plastic spherical contact problems. *Wear*, *319*(1–2), 110–117.

O'Sullivan, C. (2011). Particle-based discrete element modeling: Geomechanics perspective. *International Journal of Geomechanics*, *11*(6), 449–464.

Powers, M. C. (1982). *Comparison chart for estimating roundness and sphericity*. AGI data sheet, (Vol. 18). Alexandria, VA: American Geological Institute.

Rickman, D., McLemore, C., & Fikes, J. (2007). *Characterization summary of JSC-1A bulk lunar mare regolith simulant*. Washington, DC: National Aeronautics and Space Administration.

Saltiel, S., Bonner, B. P., Mittal, T., Delbridge, B., & Ajo-Franklin, J. B. (2017). Experimental evidence for dynamic friction on rock fractures from frequency-dependent nonlinear hysteresis and harmonic generation. *Journal of Geophysical Research: Solid Earth*, *122*, 4982–4999. https://doi.org/10.1002/2017JB014219

Sandeep, C. S., He, H., & Senetakis, K. (2018). An experimental micromechanical study of sand grain contacts behavior from different geological environments. *Engineering Geology*, *264*, 176–186.
Sandeep, C. S., & Senetakis, K. (2018a). Grain-scale mechanics of quartz sand under normal and tangential loading. *Tribology International*, *117*, 261–271.
Sandeep, C. S., & Senetakis, K. (2018b). Effect of Young's modulus and surface roughness on the inter-particle friction of granular materials. *Materials*, *11*(2), 217.
Sandeep, C. S., & Senetakis, K. (2018c). The tribological behavior of two potential-landslide saprolitic rocks. *Pure and Applied Geophysics*. https://doi.org/10.1007/s00024-018-1939-1
Sandeep, C. S., & Senetakis, K. (2018d). Influence of morphology on the micromechanical behavior of soil grain contacts. *Geomechanics and Geophysics for Geo-Energy and Geo-Resources.*. https://doi.org/10.1007/s40948-018-0094-6
Sandeep, C. S., & Senetakis, K. (2019). An experimental investigation of the microslip displacement of geological materials. *Computers and Geotechnics*, *107*, 55–67.
Sandeep, C. S., Todisco, M. C., Nardelli, V., Senetakis, K., Coop, M. R., & Lourenco, S. D. N. (2018). A micromechanical experimental study of highly/completely decomposed tuff granules. *Acta Geotechnica*. https://doi.org/10.1007/s11440-018-0656-3
Sazzad, M. M., & Suzuki, K. (2011). Effect of interparticle friction on the cyclic behavior of granular materials using 2D DEM. *Journal of Geotechnical and Geoenvironmental Engineering*, *137*(5), 545–549.
Senetakis, K., & Coop, M. (2014). The development of a new micromechanical inter-particle loading apparatus. *Geotechnical Testing Journal*, *37*(6), 1028–1039.
Senetakis, K., Coop, M. R., & Todisco, M. C. (2013a). The inter-particle coefficient of friction at the contacts of Leighton Buzzard sand quartz minerals. *Soils and Foundations*, *53*(5), 746–755.
Senetakis, K., Coop, M. R., & Todisco, M. C. (2013b). Tangential load–deflection behaviour at the contacts of soil particles. *Geotechnique Letters*, *3*(2), 59–66.
Senetakis, K., Sandeep, C. S., & Todisco, M. C. (2017). Dynamic inter-particle friction of crushed limestone surfaces. *Tribology International*, *111*, 1–8.
Soga, K., & O'Sullivan, C. (2010). Modeling of geomaterials behavior. *Soils and Foundations*, *50*(6), 861–875.
Sture, S., Costes, N. C., Batiste, S. N., Lankton, M. R., AlShibli, K. A., Jeremic, B., et al. (1998). Mechanics of granular materials at low effective stresses. *Journal of Aerospace Engineering*, *11*(3), 67–72.
Suescun-Florez, E., Roslyakov, S., Iskander, M., & Baamer, M. (2014). Geotechnical properties of BP-1 lunar regolith simulant. *Journal of Aerospace Engineering*, *28*(5), 04014124.
Sullivan, R., Anderson, R., Biesiadecki, J., Bond, T., & Stewart, H. (2011). Cohesions, friction angles, and other physical properties of Martian regolith from Mars Exploration Rover wheel trenches and wheel scuffs. *Journal of Geophysical Research*, *116*, E02006. https://doi.org/10.1029/2010JE003625
Todisco, M. C., Wang, W., Coop, M. R., & Senetakis, K. (2017). Multiple contact compression tests on sand particles. *Soils and Foundations*, *57*(1), 126–140.
Wang, D., Xu, C., Fan, X., & Wan, Q. (2018). Reduced-order modeling approach for frictional stick-slip behaviors of joint interface. *Mechanical Systems and Signal Processing*, *103*, 131–138.
Winters, W. J., Waite, W. F., Mason, D. H., Gilbert, L. Y., & Pecher, I. A. (2007). Methane gas hydrate effect on sediment acoustic and strength properties. *Journal of Petroleum Science and Engineering*, *56*(1–3), 127–135.
Yan, Z., Wilkinson, S. K., Stitt, E. H., & Marigo, M. (2015). Discrete element modelling (DEM) input parameters: Understanding their impact on model predictions using statistical analysis. *Computational Particle Mechanics*, *2*(3), 283–299.
Yimsiri, S., & Soga, K. (2000). Micromechanics-based stress–strain behaviour of soils at small strains. *Geotechnique*, *50*(5), 559–571. https://doi.org/10.1680/geot.2000.50.5.559
Yohannes, B., Hsu, L., Dietrich, W. E., & Hill, K. M. (2012). Boundary stresses due to impacts from dry granular flows. *Journal of Geophysical Research*, *117*, F02027. https://doi.org/10.1029/2011JF002150